

Postbuckling and Mode Jumping Analysis of Composite Laminates Using an Asymptotically Correct, Geometrically Nonlinear Theory

Hui Chen and Wenbin Yu

*Department of Mechanical and Aerospace Engineering, Utah State University,
Logan, Utah 84322-4130, USA*

Abstract

An analytic method is presented in this paper to study the postbuckling and mode jumping behavior of bi-axially compressed composite laminates. The governing partial differential equations (PDEs) are derived rigorously from an asymptotically correct, geometrically nonlinear theory. A novel and relatively simpler solution approach is developed to solve the two coupled fourth-order PDEs, namely, the compatibility equation and the dynamic governing equation. The generalized Galerkin method is used to solve boundary value problems corresponding to antisymmetric angle-ply and cross-ply composite plates, respectively. The variety of possible modal interactions is expressed in an explicit and concise form by transforming the coupled nonlinear governing equations into a system of nonlinear ordinary differential equations (ODEs).

The comparison between the present method and the finite element analysis (FEA) shows a pretty good match in their numerical results in the primary postbuckling region. While the FEA may lose its convergence when solution comes close the secondary bifurcation point, the analytic approach has the capability of exploring deeply into the post-secondary buckling realm and capture the mode jumping phenomenon for various combinations of plate configurations and in-plane boundary conditions. Free vibration along the stable primary postbuckling and the jumped equilibrium paths are also studied.

Key words: Composite; Laminates; Postbuckling; Mode Jumping; VAPAS

Email address: wenbin.yu@usu.edu (Wenbin Yu).

URL: www.mae.usu.edu/faculty/wenbin (Wenbin Yu).

1 Introduction

The phenomenon that thin plates under the action of elastic stresses may demonstrate a sudden dynamic change of their buckling modes when loaded deeply into the postbuckling regime is often called mode jumping. It has been proven to be of paramount importance in explaining a number of phenomenon at many different scales. Examples may be found in biophysics (e.g. membrane shape, vesicle confinement, retina detachment) [1], mechanics (e.g. compressive plates [2], shells [3], and composite laminated panels [4]), film delamination [5], and material science (e.g. thermal barrier coatings and heteroepitaxial growth of microelectronic films) [6], to cite but a few.

Inspired by Stein's first observation of such dynamic snapping phenomenon in a test of a uniformly compressed multi-bay aluminum plate, tremendous research has been dedicated to study the secondary instability and mode jumping phenomenon for isotropic plates, shells and stiffened panels.

Many of the previous analytic efforts exploring the mechanically loaded plates are carried out by using modal approximations. This has been successfully used to predict the type of the coupled solution path [7], and the possible mode jumping for various boundary conditions. In [8], the analytic results based upon carefully selected mode shapes are compared with Stein's experimental data, although the general limitations of the method red are not fully explored. The expansion of results obtained from a particular aspect ratio to a range of plate length has been achieved in [9] and [10], where the mode jumping in the buckling of struts and plates for a set of particular boundary conditions is studied and results are presented using the parametric space of redArnold tongues. Bi-axially loaded plates have recently been used to study the pattern formation and evolution of thin metal films and coatings sustaining high compressive stresses. In [5], the secondary buckling patterns of an infinite long polycarbonate strip is investigated by solving the von redKármán plate theory through a modal analysis approach, where the configuration of the plate is assumed to consist of three fundamental modes: the straight side blister mode, the bump mode and the antisymmetrical droplets, and various secondary buckling patterns have been predicted and confirmed by experimental data. The investigation is broadened from the static approach to dynamics and from mechanical loading situations to those of thermal in [11], where a complete set of mode base is used to solve the coupled nonlinear partial differential equations (PDEs) with strong geometric nonlinearity and the contribution of arbitrary assumed mode is studied systematically.

Numerical methods such as FEA and the finite strip method (FSM) are also developed to study this complex behavior. Since it is difficult to use the static path following method to locate the disconnected stable equilibriums before and after the jump, different schemes are used to find the stable equilibrium path after the jump. One scheme is to use a guess solution which is away from the primary postbuckling equilibrium as the starting computational point for the jumped branch. After the convergence of this trial solution is achieved, a standard path following method is continued to find the jumped path [12]. Obviously this strategy is not robust and some a priori information of the target branch is needed. Another is the well-known hybrid static-dynamic method developed by Riks et al. [3]. This method uses the classical quasi-static path following approach to follow the stable primary postbuckling branch until the secondary bifurcation point is reached; then, a small load step is applied

and a transient response analysis is performed to find the remote jumped path. Although this technique has been used successfully to solve various problems, for example, the damage of a compressed sandwich panel and the mode jumping of a compressed isogrid structure, it may experience a ‘spurious convergence’ problem when the applying load is implicitly coupled with the plate deformation [13]. In [14] and [13], the local post-secondary buckling behavior is investigated by using an asymptotic finite element method while the global behavior of mode jumping and postbuckling dynamics are analyzed using a non-stationary or quasi-dynamic sweeping scheme.

Just like their isotropic counterparts, compressively stressed laminated composite plates and stiffened panels demonstrate large strength reservations beyond the primary buckling load. Numerous experiments and numerical simulations have been conducted to explore the postbuckling response of such structures, see, for example, [15], [16], and [17]. Mode jumping of composite structures has been frequently reported in experiments ([18],[19], [4], and [12]). However, among the corresponding numerical comparison studies, only numerical methods in the last two papers are found to be able to successfully predict this phenomenon. Recently, a benchmark test of a 4-blade stiffened curved composite panel is conducted by redGerman Aerospace Center (DLR) and finite element simulations (carried out by using MSC.Nastran, Abaqus/Standard, and LS-Dyna) are performed to compare with the experimental data [19]. The panel is loaded deeply in the postbuckling region and mode jumping is observed at the tertiary bifurcation point in the experiment. In contrast, numerical simulations using various commercial FEA softwares fail to predict the snapping phenomenon, even though full dynamic redsimulations have been performed. This suggests that numerical difficulty still comes from the discontinuity of the stable equilibrium paths before and after mode jumping.

In this paper, a mathematically rigorous approach is adopted to investigate the the post-buckling response and mode jumping of both simply-supported antisymmetric angle-ply and cross-ply laminated composite plates. Kinematic relations and dynamic governing PDEs of composite laminates are derived rigorously from an asymptotically correct geometrically nonlinear theory. A novel and relatively simpler solution approach is developed to solve the two coupled fourth-order PDEs, namely, the compatibility equation and the dynamic governing equation. Generalized Galerkin methods are used to solve boundary value problems corresponding to antisymmetric angle-ply and cross-ply composite plates. Various postbuckling patterns of different complexity are explored before and after the mode jumping. Natural frequencies of the buckled composite plate are calculated along the stable primary postbuckling and the jumped equilibrium paths.

2 Asymptotically Correct Geometrically Nonlinear Plate Theory

Many engineering structures made with composite materials have one dimension much smaller than the other two and can be modeled as plates. Plate models are generally derived from three-dimensional (3D) elasticity theory, making use of the fact that the plate is thin in some sense. Although it is plausible to take into account the smallness of the thickness of such structures, red to construct an accurate two-dimensional (2D) model for a 3D body still introduces a lot of challenges. One can appreciate this by reading several recent papers [20–22]. Most models in the literature, for example [23–26], are based on *ad hoc* kinematic

assumptions that cannot be reasonably justified for composite structures, such as an *a priori* distribution of displacement through the thickness.

Mathematically, the approximation in constructing plate models stems from elimination of the thickness coordinate from the original 3D formulation, a dimensional reduction process red which is inevitably approximate if one wants to take advantage of the smallness of the thickness to simplify the analysis. However, other approximations that are not absolutely necessary should be avoided. For example, for geometrically nonlinear analysis of plates, it is reasonable to assume that the thickness, h , is small compared to the wavelength of deformation of the reference surface, l , and the strains are small. However, it is not at all reasonable to assume *a priori* some *ad hoc* displacement field, although that is the way most plate theories are constructed.

Hamilton's extended principle for the dynamics of a 3D body can be written as:

$$\int_{t_1}^{t_2} \int_v [\delta(\mathcal{K} - \mathcal{U}) + \overline{\delta\mathcal{W}}] dv dt = \overline{\delta\mathcal{A}}, \quad (1)$$

where δ is the variation symbol, v denotes the volume of the undeformed body, t_α ($\alpha = 1, 2$) are arbitrary fixed times, \mathcal{K} and \mathcal{U} are the kinetic and strain energy density, respectively, $\overline{\delta\mathcal{W}}$ is the virtual work of applied loads, and $\overline{\delta\mathcal{A}}$ is the virtual action at the boundary of the body. Here we follow the common practice of using Hamilton's principle to prescribe motion at t_α so that the virtual action done at the ends of time intervals vanishes. The bars on the last two quantities indicate that they may not be variations of any functionals. To circumvent the difficulty associated with 3D formulations, we can use the variational asymptotic method [27] to mathematically reduce the 3D expressions to their two dimensional counterparts as shown in [28] through an asymptotical expansion of the variational statements in terms of the following two small parameters:

$$\frac{h}{l} \ll 1 \text{ and } \frac{h}{c t_c} \ll 1, \quad (2)$$

where $red t_c$ is the characteristic scale of change of displacements in time and c is the minimal velocity of plane waves in the composite material under consideration. The first small parameter is the geometric feature of plate and the second small parameter implies that we consider only low-frequency vibrations of composite plates. After dimensional reduction, the Hamilton's extended principle can be reformulated for the plate reference plane as:

$$\int_{t_1}^{t_2} \int_\Omega [\delta(\mathcal{K}_{2D} - \mathcal{U}_{2D}) + \overline{\delta\mathcal{W}}_{2D}] d\Omega dt = \overline{\delta\mathcal{A}}_{2D}, \quad (3)$$

where Ω denotes the reference plane, \mathcal{K}_{2D} and \mathcal{U}_{2D} are the kinetic and strain energies per unit area, $\overline{\delta\mathcal{W}}_{2D}$ is the virtual work of applied loads, and $\overline{\delta\mathcal{A}}_{2D}$ is the virtual action at the boundary of plate. Although the theoretical details are given in other papers [28–30], we listed the final results here for completeness.

From the zeroth-order approximation, the kinetic and strain energies per unit area are

$$\mathcal{K}_{2D} = \frac{1}{2} \mu_{red} (\dot{U}_1^2 + \dot{U}_2^2 + \dot{U}_3^2) \quad (4)$$

$$\mathcal{U}_{2D} = \frac{1}{2} \begin{Bmatrix} \epsilon \\ \kappa \end{Bmatrix}^T \begin{bmatrix} A & B \\ B^T & D \end{bmatrix} \begin{Bmatrix} \epsilon \\ \kappa \end{Bmatrix}, \quad (5)$$

where μ is the mass per unit area, $red U_1, U_2, U_3$ are the displacements of reference plane in a chosen Cartesian coordinate system, dot over the symbol denotes time derivative, $\epsilon^T = [\epsilon_{11} \ 2\epsilon_{12} \ \epsilon_{22}]$ are the in-plane strains; and $\kappa^T = [\kappa_{11} \ 2\kappa_{12} \ \kappa_{22}]$ are the curvatures. The A , B , and D matrices can be calculated using VAPAS [28] and they are the same as those of Classical Lamination Theory (CLT). However, the *ad hoc* kinematic assumptions usually associated with CLT, such as *red* (a) the transverse normal line remains as the normal line after deformation; (b) the transverse normal is infinitely rigid in the thickness direction; and (c) the transverse normal stress is negligible, are not invoked in VAPAS. The 2D strain energy in Eq. (5) implies the following definition of plate stress and moment resultants:

$$\begin{Bmatrix} N \\ M \end{Bmatrix} = \begin{bmatrix} A & B \\ B^T & D \end{bmatrix} \begin{Bmatrix} \epsilon \\ \kappa \end{Bmatrix}, \quad (6)$$

where $N^T = [N_{11} \ N_{12} \ N_{22}]$ is the vector of in-plane forces per unit length and $M^T = [M_{11} \ M_{12} \ M_{22}]$ is the vector of bending moments per unit length.

The virtual work done by applied body forces and surface tractions and the virtual action along the boundary can be listed, respectively, as:

$$\overline{\delta \mathcal{W}}_{2D} = \delta red U_1 f_1 + \delta red U_2 f_2 + \delta red U_3 f_3 + \overline{\delta \psi}_1 m_1 + \overline{\delta \psi}_2 m_2, \quad (7)$$

$$\overline{\delta \mathcal{A}}_{2D} = - \int_{t_1}^{t_2} \int_{\Gamma} (\hat{N}_{\nu\nu} \delta red U_{\nu} + \hat{N}_{\nu\tau} \delta red U_{\tau} + \hat{N}_{\nu 3} \delta red U_3 + \hat{M}_{\nu\nu} \overline{\delta \psi}_{\nu} + \hat{M}_{\nu\tau} \overline{\delta \psi}_{\tau}) d\Gamma dt = 0, \quad (8)$$

where f_1, f_2, f_3 and m_1, m_2 can be calculated from body forces and the applied tractions on boundary surfaces in the modeling process, see [28]; $\overline{\delta \psi}_1, \overline{\delta \psi}_2$ are virtual rotations. Along the boundary curve Γ , we specify a force resultant $\hat{N}_{\nu\nu}$ and a moment resultant $\hat{M}_{\nu\nu}$ along the outward normal of Γ in the reference plane ν , with $\hat{N}_{\nu\tau}, \hat{M}_{\nu\tau}$ along the tangent of the boundary curve τ and $\hat{N}_{\nu 3}$ along the normal of the reference plane. The virtual quantities $\delta red U_{\nu}, \delta red U_{\tau}, \overline{\delta \psi}_{\nu}, \overline{\delta \psi}_{\tau}$ associated with Γ can be calculated from $\delta red U_1, \delta red U_2, \overline{\delta \psi}_1, \overline{\delta \psi}_2$ through simple transformations.

It has been shown in [28] that Eq. (3) along with Eqs. (4), (5), (7), and (8), provides an approximation of Eq. (1) asymptotically correct up to the order of h^0/l^0 and $h^0/(c\tau)^0$.

Although this plate theory allows an exact description of geometry, a geometrically-exact theory such as that derived in [29] is unnecessarily overcomplex in studying postbuckling and mode jumping of composite plates. To this end, we specialize the geometrically-exact theory in [29] according to the kinematic assumption that strains are much smaller than the rotations, which is similar to the assumption used in von Kármán theory for isotropic plates.

This assumption helps us to simplify the expressions for plate strains as

$$\begin{aligned}
\epsilon_{11} &= U_{1,1} + \frac{1}{2}U_{3,1}^2, \\
2\epsilon_{12} &= U_{1,2} + U_{2,1} + U_{3,1}U_{3,2}, \\
\epsilon_{22} &= U_{2,2} + \frac{1}{2}U_{3,2}^2, \\
\kappa_{11} &= -U_{3,11}, \\
\kappa_{12} &= -U_{3,12}, \\
\kappa_{22} &= -U_{3,22},
\end{aligned} \tag{9}$$

and the virtual rotations can be simply expressed in terms of displacements as

$$\bar{\delta}\psi_1 = -\delta red U_{3,1} \quad \bar{\delta}\psi_2 = -\delta red U_{3,2}. \tag{10}$$

Aided with these expressions, one can derive the equations of motion from Eq. (3) as

$$\begin{aligned}
N_{11,1} + N_{12,2} + f_1 &= \mu\ddot{U}_1, \\
N_{12,1} + N_{22,2} + f_2 &= \mu\ddot{U}_2, \\
M_{11,11} + 2M_{12,12} + M_{22,22} + N_p + f_3 + m_{1,1} + m_{2,2} &= \mu\ddot{U}_3,
\end{aligned} \tag{11}$$

with

$$N_p = (N_{11}U_{3,1} + N_{12}U_{3,2})_{,1} + (N_{12}U_{3,1} + N_{22}U_{3,2})_{,2}. \tag{12}$$

The geometry boundary conditions can be trivially specified, and the applied forces and moments associated with the natural boundary conditions on the boundary curve Γ are

$$\begin{aligned}
\hat{N}_{\nu\nu} &= n_1^2 N_{11} + 2n_1 n_2 N_{12} + n_2^2 N_{22}, \\
\hat{N}_{\nu\tau} &= n_1 n_2 (N_{22} - N_{11}) + (n_1^2 - n_2^2) N_{12}, \\
\hat{N}_{\nu 3} + \hat{M}_{\nu\tau, \tau} &= (N_{11}U_{3,1} + N_{12}U_{3,2} + M_{11,1} + M_{12,2})n_1, \\
&\quad + (N_{12}U_{3,1} + N_{22}U_{3,2} + M_{12,1} + M_{22,2})n_2 + m_1 n_1 + m_2 n_2 + M_{\nu\tau, \tau}, \\
\hat{M}_{\nu\nu} &= M_{\nu\nu},
\end{aligned} \tag{13}$$

where $n_1 = \cos \phi$, $n_2 = \sin \phi$, ϕ is the angle between the outward normal of the boundary and x_1 direction, and

$$M_{\nu\nu} = n_1^2 M_{11} + 2n_1 n_2 M_{12} + n_2^2 M_{22}, \quad M_{\nu\tau} = n_1 n_2 (M_{22} - M_{11}) + (n_1^2 - n_2^2) M_{12}. \tag{14}$$

3 Analytic Solutions

One of the goals of the present work is to seek analytic solutions for the generalized asymptotically correct, geometrically nonlinear composite plate theory, particularly for postbuckling analysis and mode jumping analysis. To this end, we only focus on bi-axially compressed, simply-supported rectangular plates without in-plane distributed loads, $f_1 = f_2 = 0$, and considering the in-plane red accelerations, \ddot{U}_1 and \ddot{U}_2 , negligible in comparison to \ddot{U}_3 . The

plate under investigation is sketched in Fig. 1. For illustrative purpose, we provide detailed formulations for antisymmetric angle-ply and cross-ply laminates. As it will be clear in the following derivation, the method developed in this paper actually provides a general way to deal with both in-plane and out-of-plane boundary conditions and can be readily extended to analyze composite plates with arbitrary lamination schemes.

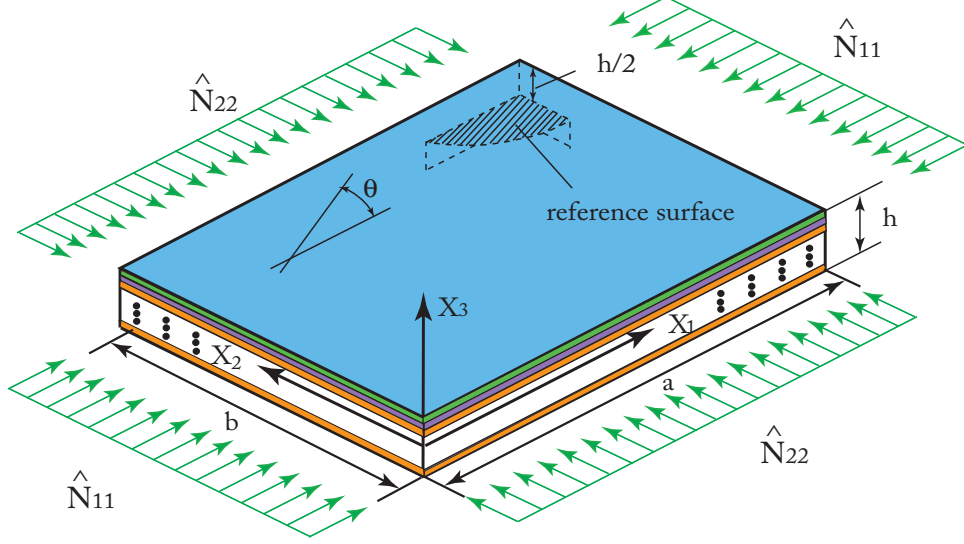


Fig. 1. Schematic of laminated plates

3.1 Governing differential equations for laminated composite plates

With the constitutive relations for the laminated composite plate obtained in Eq. (6), its partial inverse takes the form of

$$\begin{Bmatrix} \varepsilon \\ M \end{Bmatrix} = \begin{bmatrix} A^* & B^* \\ H^* & D^* \end{bmatrix} \begin{Bmatrix} N \\ \kappa \end{Bmatrix}, \quad (15)$$

where, $A^* = A^{-1}$, $B^* = -A^{-1}B$, $H^* = -B^{*T}A^{-1}$, and $D^* = D - B^T A^{-1} B$.

By introducing an Airy stress function defined by:

$$N_{11} = F_{,22}, \quad N_{12} = -F_{,12}, \quad \text{and} \quad N_{22} = F_{,11},$$

one can derive the von Kármán compatibility equation for generalized composite laminated plates from the first three equations of Eq. (9) as

$$\begin{aligned} & A_{22}^* F_{,1111} + (2A_{12}^* + A_{66}^*) F_{,1122} + A_{11}^* F_{,2222} - 2A_{26}^* F_{,1112} - 2A_{16}^* F_{,1222} = \\ & U_{3,12}^2 - U_{3,11} U_{3,22} + B_{21}^* U_{3,1111} + (B_{11}^* - 2B_{66}^* + B_{22}^*) U_{3,1122} + B_{12}^* U_{3,2222} \\ & + (2B_{26}^* - B_{61}^*) U_{3,1112} + (2B_{16}^* - B_{62}^*) U_{3,1222}. \end{aligned} \quad (16)$$

One can easily check that the Airy stress function automatically satisfy the first two equations of motion in Eq. (11) with aforementioned specialization and assumptions. The last equation

in Eq. (11) can now be rewritten as

$$\begin{aligned}
& \mu\ddot{U}_3 + D_{11}^* U_{3,1111} + 2(D_{12}^* + 2D_{66}^*)U_{3,1122} + D_{22}^* U_{3,2222} + 4D_{16}^* U_{3,1112} \\
& + 4D_{26}^* U_{3,1222} + B_{21}^* F_{,1111} + (B_{11}^* - 2B_{66}^* + B_{22}^*)F_{,1122} \\
& + B_{12}^* F_{,2222} + (2B_{26}^* - B_{61}^*)F_{,1112} + (2B_{16}^* - B_{62}^*)F_{,1222} \\
& = f_3 + F_{,22}U_{3,11} - 2F_{,12}U_{3,12} + F_{,11}U_{3,22},
\end{aligned} \tag{17}$$

where f_3 denotes total transverse load per unit area and no distributed moments are applied in the plate.

It is noted that the significant difference of the order of the magnitude of coefficients in above dimensional PDEs may cause convergence problem when tracing the postbuckling paths through bifurcation points. This can be avoided by introducing the following dimensionless quantities (indicated by a tilde):

$$\begin{aligned}
\tilde{x}_1 &= \frac{x_1}{a}, & \tilde{x}_2 &= \frac{x_2}{a}, & \tilde{U}_3 &= \frac{U_3}{\sqrt{A_{22}^* D_{11}^*}}, & r &= b/a, \\
\tilde{F} &= \frac{F}{D_{11}^*}, & \tilde{f}_3 &= \frac{a^4 f_3}{D_{11}^* \sqrt{D_{11}^* A_{22}^*}}, & \tilde{t} &= \sqrt{\frac{D_{11}^*}{a^4 \mu}} t,
\end{aligned} \tag{18}$$

where r is the aspect ratio of the plate and \tilde{t} denotes the non-dimensional time. The dimensionless compatibility and governing equations now take the form of

$$\begin{aligned}
& \tilde{A}_{22} \tilde{F}_{,\tilde{1}\tilde{1}\tilde{1}\tilde{1}} + (2\tilde{A}_{12} + \tilde{A}_{66}) \tilde{F}_{,\tilde{1}\tilde{1}\tilde{2}\tilde{2}} + \tilde{A}_{11} \tilde{F}_{,\tilde{2}\tilde{2}\tilde{2}\tilde{2}} - 2\tilde{A}_{26} \tilde{F}_{,\tilde{1}\tilde{1}\tilde{1}\tilde{2}} - 2\tilde{A}_{16} \tilde{F}_{,\tilde{1}\tilde{2}\tilde{2}\tilde{2}} = \\
& \tilde{U}_{3,\tilde{1}\tilde{2}}^2 - \tilde{U}_{3,\tilde{1}\tilde{1}} \tilde{U}_{3,\tilde{2}\tilde{2}} + \tilde{B}_{21} \tilde{U}_{3,\tilde{1}\tilde{1}\tilde{1}\tilde{1}} + (\tilde{B}_{11} - 2\tilde{B}_{66} + \tilde{B}_{22}) \tilde{U}_{3,\tilde{1}\tilde{1}\tilde{2}\tilde{2}} + \tilde{B}_{12} \tilde{U}_{3,\tilde{2}\tilde{2}\tilde{2}\tilde{2}} \\
& + (2\tilde{B}_{26} - \tilde{B}_{61}) \tilde{U}_{3,\tilde{1}\tilde{1}\tilde{1}\tilde{2}} + (2\tilde{B}_{16} - \tilde{B}_{62}) \tilde{U}_{3,\tilde{1}\tilde{2}\tilde{2}\tilde{2}},
\end{aligned} \tag{19}$$

and

$$\begin{aligned}
& \tilde{U}_3'' + \tilde{D}_{11} \tilde{U}_{3,\tilde{1}\tilde{1}\tilde{1}\tilde{1}} + 2(\tilde{D}_{12} + 2\tilde{D}_{66}) \tilde{U}_{3,\tilde{1}\tilde{1}\tilde{2}\tilde{2}} + \tilde{D}_{22} \tilde{U}_{3,\tilde{2}\tilde{2}\tilde{2}\tilde{2}} + 4\tilde{D}_{16} \tilde{U}_{3,\tilde{1}\tilde{1}\tilde{1}\tilde{2}} \\
& + 4\tilde{D}_{26} \tilde{U}_{3,\tilde{1}\tilde{2}\tilde{2}\tilde{2}} + \tilde{B}_{21} \tilde{F}_{,\tilde{1}\tilde{1}\tilde{1}\tilde{1}} + (\tilde{B}_{11} - 2\tilde{B}_{66} + \tilde{B}_{22}) \tilde{F}_{,\tilde{1}\tilde{1}\tilde{2}\tilde{2}} \\
& + \tilde{B}_{12} \tilde{F}_{,\tilde{2}\tilde{2}\tilde{2}\tilde{2}} + (2\tilde{B}_{26} - \tilde{B}_{61}) \tilde{F}_{,\tilde{1}\tilde{1}\tilde{1}\tilde{2}} + (2\tilde{B}_{16} - \tilde{B}_{62}) \tilde{F}_{,\tilde{1}\tilde{2}\tilde{2}\tilde{2}} \\
& = \tilde{f}_3 + \tilde{F}_{,\tilde{2}\tilde{2}} \tilde{U}_{3,\tilde{1}\tilde{1}} - 2\tilde{F}_{,\tilde{1}\tilde{2}} \tilde{U}_{3,\tilde{1}\tilde{2}} + \tilde{F}_{,\tilde{1}\tilde{1}} \tilde{U}_{3,\tilde{2}\tilde{2}},
\end{aligned} \tag{20}$$

where $()'' = \partial^2()/\partial\tilde{t}^2$, $\tilde{A} = (1/A_{22}^*)A^*$, $\tilde{B} = (1/\sqrt{A_{22}^* D_{11}^*}) B^*$, and $\tilde{D} = (1/D_{11}^*)D^*$.

With further introducing the following additional dimensionless relations,

$$\begin{aligned}
\tilde{U}_1 &= \frac{a}{A_{22}^* D_{11}^*} U_1, & \tilde{U}_2 &= \frac{a}{A_{22}^* D_{11}^*} U_2, & \tilde{\varepsilon} &= \frac{a^2}{A_{22}^* D_{11}^*} \varepsilon, \\
\tilde{\kappa} &= \frac{a^2}{\sqrt{A_{22}^* D_{11}^*}} \kappa, & \tilde{N} &= \frac{a^2}{D_{11}^*} N, & \tilde{M} &= \frac{a^2}{D_{11}^* \sqrt{A_{22}^* D_{11}^*}} M, \\
\tilde{A}_A &= A_{22}^* A, & \tilde{B}_B &= \frac{A_{22}^*}{\sqrt{A_{22}^* D_{11}^*}} B, & \tilde{D}_D &= \frac{1}{D_{11}^*} D,
\end{aligned} \tag{21}$$

all the previously derived physical relations, such as kinematic relations in Eqs. (9) and (10) and constitutive laws in Eqs. (6) and (15) still hold their original formats without changes.

Thus, by carefully selecting the nondimensionalization scheme, not only can the equation coefficients be re-scaled to the same order, but also their physical meanings could be retained.

For simplicity, except for such dimensionless coefficients as in \tilde{A} , \tilde{B} , and \tilde{D} matrices, we use the dimensionless values and drop the tilde throughout the rest of the paper.

3.2 Boundary conditions

In order to describe in-plane boundary conditions, the in-plane forces, \hat{N}_{11} , \hat{N}_{22} , applied along the plate edges are each partitioned into two parts: the uniformly distributed forces, \bar{N}_{11} or \bar{N}_{22} , and the variational one, $F_{,22}^p(x_1, x_2)$ or $F_{,11}^p(x_1, x_2)$, *i.e.*,

$$\hat{N}_{11} = \bar{N}_{11} + F_{,22}^p(x_1, x_2), \quad \hat{N}_{22} = \bar{N}_{22} + F_{,11}^p(x_1, x_2), \quad (22)$$

where, $F^p(x_1, x_2)$ is the particular solution of the compatibility equation and explicit expressions will be given in the next subsection for specific cases.

Two types of boundary conditions are usually considered in dealing with buckling and post-buckling analysis, namely, the redstraight-edge (constant end shortening) one (23) and the uniformly distributed compressive load one (24):

$$\begin{aligned} U_3 = \hat{N}_{12} = \hat{M}_{11} = 0, \quad U_1 = \text{constant}, \quad \text{at } x_1 = 0, 1, \\ U_3 = \hat{N}_{12} = \hat{M}_{22} = 0, \quad U_2 = \text{constant}, \quad \text{at } x_2 = 0, r, \end{aligned} \quad (23)$$

and

$$\begin{aligned} U_3 = \hat{N}_{12} = \hat{M}_{11} = 0, \quad \hat{N}_{11} = -\bar{N}_{11}, \quad \text{at } x_1 = 0, 1, \\ U_3 = \hat{N}_{12} = \hat{M}_{22} = 0, \quad \hat{N}_{22} = -\bar{N}_{22}, \quad \text{at } x_2 = 0, r. \end{aligned} \quad (24)$$

It is clear by setting the constant in (23) equal to zero, one gets the in-plane, fixed-edge boundary condition. In the present study, without loss of generality, we will apply the redstraight-edge boundary condition for antisymmetric angle-ply laminates and the load-distribution one for cross-ply laminates.

3.3 Transformation to nonlinear ODEs

Now, our nonlinear analysis becomes to solve two coupled PDEs, Eq. (19) and Eq. (20), subjected to boundary conditions in either Eq. (23) or Eq. (24). This is certainly not a trivial problem, particularly, if one want to seek analytic solutions. We will rely on Fourier series expansion to transform the PDEs into ordinary differential equations (ODEs). We will illustrate how this can be achieved for both antisymmetric angle-ply and cross-ply laminates.

3.3.1 Angle-ply laminates

For antisymmetric angle-ply laminated plates, some components in \tilde{A} , \tilde{B} , and \tilde{D} are always zero, therefore, the compatibility equation and the governing equation in Eqs. (19) and (20)

can be simplified as:

$$\begin{aligned} & \tilde{A}_{22}F_{,1111} + (2\tilde{A}_{12} + \tilde{A}_{66})F_{,1122} + \tilde{A}_{11}F_{,2222} = \\ & U_{3,12}^2 - U_{3,11}U_{3,22} + (2\tilde{B}_{26} - \tilde{B}_{61})U_{3,1112} + (2\tilde{B}_{16} - \tilde{B}_{62})U_{3,1222}, \end{aligned} \quad (25)$$

$$\begin{aligned} & U_3'' + \tilde{D}_{11}U_{3,1111} + 2(\tilde{D}_{12} + 2\tilde{D}_{66})U_{3,1122} + \tilde{D}_{22}U_{3,2222} + (2\tilde{B}_{26} - \tilde{B}_{61})F_{,1112} \\ & + (2\tilde{B}_{16} - \tilde{B}_{62})F_{,1222} = f_3 + F_{,22}U_{3,11} - 2F_{,12}U_{3,12} + F_{,11}U_{3,22}. \end{aligned} \quad (26)$$

For out-of-plane, simply-supported laminated plates, the transverse deflection w can be expressed as double Fourier series:

$$U_3 = \sum_{k,l} W_{kl} \sin k\pi x_1 \sin \frac{l\pi x_2}{r}, \quad (27)$$

where W_{kl} represents the amplitude of the buckling mode with k and l half-waves over the longitudinal and the lateral directions, respectively; odd values of the subscripts k and l denote symmetric modes while even values denote the antisymmetric ones.

Using the Fourier expansion in Eq. (27), one can transform the two coupled spatial-temporal PDEs which govern the dynamic postbuckling behavior of the composite laminates to a system of nonlinear ODEs governing the modal amplitude. To achieve this, we need to deal with the compatibility equation first. In view of Eq. (22), we assume that the solution of Eq. (25) also contains a homogeneous solution $F^h(x_1, x_2)$ and a particular solution $F^p(x_1, x_2)$, such that

$$F(x_1, x_2) = F^h(x_1, x_2) + F^p(x_1, x_2), \quad (28)$$

with

$$F^h(x_1, x_2) = -\frac{1}{2}\bar{N}_{11}x_2^2 - \frac{1}{2}\bar{N}_{22}x_1^2. \quad (29)$$

Although it may be possible to obtain the mathematically exact homogeneous solution of Eq. (25) by using a differential operator method (see, for example [31] the solution procedure for uniaxially compressed isotropic plates), this procedure is rather complex and only suitable for particular boundary conditions. Since the main purpose of the present paper is focused on studying the post-buckling and mode jumping of bi-axially compressed plates with zero shear stress at boundaries, here in Eq. (29) the homogeneous solution is assumed to take a form which has been commonly used and proved to be successful in predicting post-buckling behaviors of the uniaxially and bi-axially compressed and thermally buckled isotropic plates, [9–11,32]. Substituting Eq. (27) into Eq. (25) and carrying out some algebraic and calculus operations, one may obtain the particular solution of the compatibility equation as

$$F^p(x_1, x_2) = \left(\frac{r^2}{4}\right) \sum_{k,l,m,n} W_{kl}W_{mn}S_{1x}^T C_{klmn}S_{1y} + \sum_{k,l} W_{kl} c_{5kl} \cos(k\pi x_1) \cos\left(\frac{l\pi x_2}{r}\right), \quad (30)$$

where,

$$S_{1x} = \left\{ \begin{array}{l} \cos((k+m)\pi x_1) \\ \cos((k-m)\pi x_1) \end{array} \right\}, \quad C_{klmn} = \begin{bmatrix} c_1 & c_2 \\ c_3 & c_4 \end{bmatrix}, \quad S_{1y} = \left\{ \begin{array}{l} \cos\left(\frac{(l+n)\pi x_2}{r}\right) \\ \cos\left(\frac{(l-n)\pi x_2}{r}\right) \end{array} \right\}. \quad (31)$$

The coefficients $c_1 \sim c_4$ in matrix C_{klmn} and c_{5kl} are given by

$$\begin{aligned}
c_1 &= \frac{klmn - k^2n^2}{\tilde{A}_{22}(k+m)^4r^4 + (2\tilde{A}_{12} + \tilde{A}_{66})r^2(k+m)^2(l+n)^2 + \tilde{A}_{11}(l+n)^4} \\
c_2 &= \frac{klmn + k^2n^2}{\tilde{A}_{22}(k+m)^4r^4 + (2\tilde{A}_{12} + \tilde{A}_{66})r^2(k+m)^2(l-n)^2 + \tilde{A}_{11}(l-n)^4} \\
c_3 &= \frac{klmn + k^2n^2}{\tilde{A}_{22}(k-m)^4r^4 + (2\tilde{A}_{12} + \tilde{A}_{66})r^2(k-m)^2(l+n)^2 + \tilde{A}_{11}(l+n)^4} \\
c_4 &= \frac{klmn - k^2n^2}{\tilde{A}_{22}(k-m)^4r^4 + (2\tilde{A}_{12} + \tilde{A}_{66})r^2(k-m)^2(l-n)^2 + \tilde{A}_{11}(l-n)^4} \\
c_{5kl} &= \frac{klr \left[(\tilde{B}_{61} - 2\tilde{B}_{26})k^2r^2 + (\tilde{B}_{62} - 2\tilde{B}_{16})l^2 \right]}{\tilde{A}_{22}k^4r^4 + (2\tilde{A}_{12} + \tilde{A}_{66})(rkl)^2 + \tilde{A}_{11}l^4},
\end{aligned} \tag{32}$$

where $r = b/a$ is the aspect ratio of the plate and $c_4 = 0$ if $k = m$ and $l = n$.

It is easy to verify that the solution $F(x_1, x_2)$ automatically satisfies the zero shear force and zero moment boundary conditions along edges expressed in Eq. (23). Additionally, it can be proved that the straight-edge or the constant end-shortening boundary condition is also satisfied, see Appendix A.

Finally, the dynamic governing equation in Eq.(26) can be transformed to a series of non-linear ODEs with respect to the modal amplitude W_{kl} by using a Galerkin procedure with a weighting function $\phi_{pq}(x_1, x_2)$ taking the form of

$$\phi_{pq}(x_1, x_2) = \sin(p\pi x_1) \sin\left(\frac{q\pi x_2}{r}\right). \tag{33}$$

Letting

$$\begin{aligned}
f_u &= \tilde{D}_{11}U_{3,1111} + 2(\tilde{D}_{12} + 2\tilde{D}_{66})U_{3,1122} + \tilde{D}_{22}U_{3,2222}, \\
f_F &= (2\tilde{B}_{26} - \tilde{B}_{61})F_{,1112} + (2\tilde{B}_{16} - \tilde{B}_{62})F_{,1222}, \\
f_{Fu} &= F_{,22}U_{3,11} - 2F_{,12}U_{3,12} + F_{,11}U_{3,22}
\end{aligned} \tag{34}$$

and defining the inner product of two arbitrary functions of $f(x_1, x_2)$ and $g(x_1, x_2)$ as

$$[f(x_1, x_2), g(x_1, x_2)] \stackrel{\text{def}}{=} \int_0^a \int_0^b f(x_1, x_2)g(x_1, x_2) dx_1 dx_2, \tag{35}$$

we can transform the dynamic governing equation in Eq. (26) to be

$$[U_3'', \phi_{pq}] + [f_u, \phi_{pq}] + [f_F, \phi_{pq}] = [f_3, \phi_{pq}] + [f_{Fu}, \phi_{pq}]. \tag{36}$$

Substituting expressions for U_3 and F defined in Eqs. (27) - (30) into the above equation and performing some linear algebraic operations lead to a successful transformation of the two coupled PDEs in Eqs.(25) and (26) into a compactly formulated series of nonlinear ODEs

expressed explicitly in terms of amplitudes of corresponding buckling modes as:

$$\begin{aligned}
W''_{pq} + \left(\frac{\pi}{r}\right)^4 & \left\{ [\tilde{D}_{11}(pr)^4 + 2(\tilde{D}_{12} + 2\tilde{D}_{66})(rpq)^2 + \tilde{D}_{22}q^4] \right. \\
& \left. - c_{5pq}rpq [(2\tilde{B}_{26} - \tilde{B}_{61})(pr)^2 + (2\tilde{B}_{16} - \tilde{B}_{62})q^2] - \left(\frac{r}{\pi}\right)^2 [\bar{N}_{11}(pr)^2 + \bar{N}_{22}q^2] \right\} W_{pq} \\
& = \left(\frac{4}{r}\right) [f_3, \phi_{pq}] + \left(\frac{\pi^4}{r^2}\right) \sum_{k,l,m,n} W_{kl}W_{mn}V_{1x}^T (rL_1 + c_{5mn}G_1) V_{1y} \\
& + \left(\frac{\pi^4}{4}\right) \sum_{i,j,k,l,m,n} W_{ij}W_{kl}W_{mn}V_{2x}^T E V_{2y},
\end{aligned} \tag{37}$$

red where, coefficient vectors V_{1x} , V_{1y} , V_{2x} , V_{2y} and matrices L_1 , G_1 , E_{11} , E_{12} , and E are provided in Appendix B.

The inner product of the transverse load and the Galerkin's weighting function $[f_3, \phi_{pq}]$ takes the form of either $q_0 \sin(p\pi x_{10}) \sin(q\pi x_{20}/r)$ or $4q_0r/(pq\pi^2)$ for $p, q = 1, 3, 5, \dots$, depending on whether the vertical load is concentrated red at (x_{10}, x_{20}) or uniformly distributed.

3.3.2 Cross-ply laminates

For antisymmetric cross-ply laminated plates, zeroes existing in \tilde{A} , \tilde{B} , and \tilde{D} enable us to simplify the compatibility equation and the governing equation in Eqs. (19) and (20) as:

$$\begin{aligned}
\tilde{A}_{22}F_{,1111} + (2\tilde{A}_{12} + \tilde{A}_{66})F_{,1122} + \tilde{A}_{11}F_{,2222} = \\
U_{3,12}^2 - U_{3,11}U_{3,22} + \tilde{B}_{21}U_{3,1111} + (\tilde{B}_{11} + \tilde{B}_{22})U_{3,1122} + \tilde{B}_{12}U_{3,2222},
\end{aligned} \tag{38}$$

$$\begin{aligned}
U_3'' + \tilde{D}_{11}U_{3,1111} + 2(\tilde{D}_{12} + 2\tilde{D}_{66})U_{3,1122} + \tilde{D}_{22}U_{3,2222} + \tilde{B}_{21}F_{,1111} \\
+ (\tilde{B}_{11} + \tilde{B}_{22})F_{,1122} + \tilde{B}_{12}F_{,2222} = f_3 + F_{,22}U_{3,11} - 2F_{,12}U_{3,12} + F_{,11}U_{3,22}.
\end{aligned} \tag{39}$$

Uniformly distributed force in-plane boundary condition, Eq. (24), is considered for plate with this kind of lamination configuration.

By applying the same procedure as redwe did in the process of analyzing antisymmetric angle-ply laminates, the general solution of the compatibility equation can be expressed as

$$\begin{aligned}
F(x_1, x_2) = -\frac{1}{2}\bar{N}_{11}x_2^2 - \frac{1}{2}\bar{N}_{22}x_1^2 + \left(\frac{r^2}{4}\right) \sum_{k,l,m,n} W_{kl}W_{mn}S_{1x}^T C_{klmn}S_{1y} \\
+ \sum_{k,l} W_{kl} c_{6kl} \sin(k\pi x_1) \sin\left(\frac{l\pi x_2}{r}\right),
\end{aligned} \tag{40}$$

with coefficients c_1 , c_2 , c_3 , c_4 given by Eq. (32) and c_{6kl} given by

$$c_{6kl} = \frac{\tilde{B}_{21}(kr)^4 + (\tilde{B}_{11} + \tilde{B}_{22})(klr)^2 + \tilde{B}_{12}l^4}{\tilde{A}_{22}(kr)^4 + (2\tilde{A}_{12} + \tilde{A}_{66})(klr)^2 + \tilde{A}_{11}l^4}. \tag{41}$$

In contrast with the angle-ply situation, the general solution obtained above does not satisfy the zero resultant moment and zero shear force requirements on boundaries. Fortunately, these boundary effects can be taken into account by applying the generalized Galerkin method in the stage of transforming the dynamic governing equation.

red It can be seen from Eq. (A-5) and (A-6), the end shortenings terms along the x_1 and x_2 directions are no longer constants for antisymmetric cross-ply laminates.

By changing the definition of f_F in Eq. (34) to

$$f_F = \tilde{B}_{21}F_{,1111} + (\tilde{B}_{11} + \tilde{B}_{22})F_{,1122} + \tilde{B}_{12}F_{,2222} \quad (42)$$

and applying the generalized Galerkin method to Eq. (39), the dynamic governing equation for cross-ply laminates becomes

$$\begin{aligned} [U_3'', \phi_{pq}] + [f_u, \phi_{pq}] + [f_F, \phi_{pq}] &= [f_3, \phi_{pq}] + [f_{Fu}, \phi_{pq}] + \int_{\Gamma_\sigma} M_{nn} \frac{\partial \phi_{pq}}{\partial n} ds. \\ - \int_{\Gamma_\sigma} [(N_{nn} - (-\bar{N}_{nn})) \delta U_n + (N_{ns} - (-\bar{N}_{ns})) \delta U_s] ds, \end{aligned} \quad (43)$$

where, the first integration term represents the boundary effect of the bending moment while the last integration the in-plane force boundary effects.

The final form of the dynamic governing equation is therefore given by

$$\begin{aligned} W_{pq}'' - \left(\frac{4}{r}\right) (C_{B1}\bar{N}_{11} + C_{B2}\bar{N}_{22}) + \left(\frac{\pi}{r}\right)^4 \{ [\tilde{D}_{11}(pr)^4 + 2(\tilde{D}_{12} + 2\tilde{D}_{66})(pqr)^2 + \tilde{D}_{22}q^4] \\ + c_{6pq} [\tilde{B}_{21}(pr)^4 + (\tilde{B}_{11} + \tilde{B}_{22})(pqr)^2 + \tilde{B}_{12}q^4] - \left(\frac{r}{\pi}\right)^2 (\bar{N}_{11}(pr)^2 + \bar{N}_{22}q^2) \} W_{pq} \\ = \left(\frac{4}{r}\right) [f_3, \phi_{pq}] + \frac{\pi^4}{4} \sum_{i,j,k,l,m,n} W_{ij}W_{kl}W_{mn}V_{2x}^T E V_{2y} \\ + \left(\frac{\pi^2}{4r^2}\right) \sum_{k,l,m,n} W_{kl}W_{mn} \left[V_{3x}^T (c_{6mn}G_2 - L_2)V_{3y} + \left(\frac{16r}{\pi^2}\right) C_{L3}V_{4x}^T L_3 V_{4y} \right] \\ - \frac{4}{r} \int_{\Gamma_\sigma} [(N_{nn} + \bar{N}_{nn}) \delta U_n + (N_{ns} + \bar{N}_{ns}) \delta U_s] ds, \end{aligned} \quad (44)$$

where, coefficients C_{B1} , C_{B2} , C_{L3} , vectors V_{3x} , V_{4x} , V_{3y} , V_{4y} , matrices G_2 , L_2 , L_3 , and the expression for the in-plane force integration are provided in red Appendix B.

3.4 Buckling and postbuckling analysis

The linear buckling load for both antisymmetric angle-ply and cross-ply laminates can be readily obtained from their dynamic equations. For redperfect angle-ply composite plates, since there is no pre-buckling deflection, the linear buckling load can be obtained by simply dropping the dynamic and nonlinear terms in Eq. (37), which, in the case of uniaxially compression ($\hat{N}_{22} = 0$), gives

$$\begin{aligned} \bar{N}_{11cr} &= \frac{\pi^2}{p^2r^4} \left\{ [\tilde{D}_{11}(pr)^4 + 2(\tilde{D}_{12} + 2\tilde{D}_{66})(pqr)^2 + \tilde{D}_{22}q^4] \right. \\ &\quad \left. - c_{5pq}(pqr) [(2\tilde{B}_{26} - \tilde{B}_{61})(pr)^2 + (2\tilde{B}_{16} - \tilde{B}_{62})q^2] \right\}. \end{aligned} \quad (45)$$

If two unloaded edges are fixed in-plane, say $U_2 = 0$ at $x_2 = 0, r$, setting $\Delta_{22} = 0$ and ignoring the nonlinear terms in Eq. (A-4), we obtain a linear relationship between \bar{N}_{11} and

\bar{N}_{22} , which helps us to determine the critical buckling for the fixed-edge boundary condition as:

$$\bar{N}_{11cr} = \frac{\tilde{A}_{22}\pi^2}{(\tilde{A}_{22}p^2r^2 - \tilde{A}_{12}q^2)r^2} \left\{ \left[\tilde{D}_{11}(pr)^4 + 2(\tilde{D}_{12} + 2\tilde{D}_{66})(pqr)^2 + \tilde{D}_{22}q^4 \right] - c_{5pq}(pqr) \left[(2\tilde{B}_{26} - \tilde{B}_{61})(pr)^2 + (2\tilde{B}_{16} - \tilde{B}_{62})q^2 \right] \right\}. \quad (46)$$

For redperfect antisymmetric cross-ply laminated plates, because of the existence of pre-buckling deflection caused by non-zero coefficients C_{B1} and C_{B2} in Eq. (44), virtually no linear buckling occurs for this lamination configuration. However, nominal linear buckling load can still redbe obtained by dropping the dynamic, pre-buckling, and nonlinear terms in dynamic equation Eq. (44). The nominal critical buckling load for uniformly compressed composite plate is

$$\bar{N}_{11cr} = \frac{\pi^2}{p^2r^4} \left\{ \tilde{D}_{11}(pr)^4 + 2(\tilde{D}_{12} + 2\tilde{D}_{66})(pqr)^2 + \tilde{D}_{22}q^4 + c_{6pq} \left[\tilde{B}_{21}(pr)^4 + (\tilde{B}_{11} + \tilde{B}_{22})(pqr)^2 + \tilde{B}_{12}q^4 \right] \right\}. \quad (47)$$

red For the postbuckling analysis, here we only provide a outline of the processing procedure, interesting readers may consult [11] for more details. The amplitude equations presented in dynamic equations Eq. (37) and Eq. (44) can be rewritten in a matrix form as

$$M\ddot{W} + K_w W = f(W, \bar{N}_{11}, \bar{N}_{22}), \quad (48)$$

where W consists of amplitudes of the assumed buckling modes, M and K_w represent the corresponding mass and stiffness matrices, and $f(W, \bar{N}_{11}, \bar{N}_{22})$ denotes nonlinear terms. It is obvious that the dimensionless diagonal mass matrix $M = I$ is positive definite. Hence the dynamic stability (in the Lyapunov sense) of the equilibrium paths is determined by the sign of the smallest eigenvalue of the stiffness matrix K_w .

Parametric continuation method is used to obtained the stationary solution of the nonlinear ODEs in Eq. (48) and the stability of the equilibrium paths are determined by the positive definiteness of the stiffness matrix. A continuation package— AUTO [33] is used to follow the equilibrium path and log the bifurcation points. Natural frequencies of small amplitude free vibration along stable equilibrium paths (before and after mode jumping) are calculated by locally linearizing the nonlinear dynamic system and solving the associated eigenvalue problem. By this we can trace the characteristics of the free vibration of the composite plate before and after mode jumping.

4 Results and Discussions

In this section, red the developed method is verified by comparing its results with those available in the literature and those obtained through the finite element analysis using ANSYS. Then, we use the present method to analyze the postbuckling and mode jumping behavior for both antisymmetric angle-ply and cross-ply laminated plates with four edges simply supported out of plane.

4.1 Validation of the present method

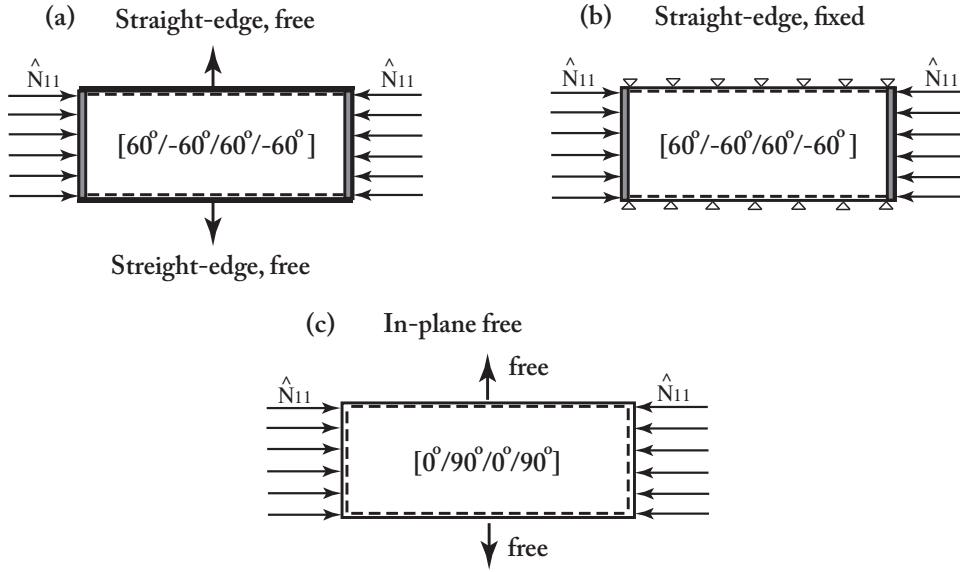


Fig. 2. Sketches of three cases investigated. (a) case 1: angle-ply laminated plate, straight-edge, two unloaded edges in-plane free; (b) case 2: angle-ply laminated plate, straight-edge, two unloaded edges in-plane fixed; (c) case 3: cross-ply laminated plate, two unloaded edges in-plane free.

Despite of the capability of the current method for analyzing bi-axially compressive plates, here we focus our analyses only on the uniaxially compressed composite plates for simplicity. As illustrated in Fig. 2, we study the following three cases:

- case 1: a $[60^\circ / -60^\circ / 60^\circ / -60^\circ]$ four-layer angle-ply plate, with two unloaded edges remaining straight and free in plane; see Eq. (23) and Fig. 2 red(a).
- case 2: a $[60^\circ / -60^\circ / 60^\circ / -60^\circ]$ four-layer angle-ply plate, with two unloaded edges remaining straight and fixed in plane; see Eq. (23) and Fig. 2 red(b).
- case 3: a $[90^\circ / 0^\circ / 90^\circ / 0^\circ]$ four-layer cross-ply plate with in-plane free condition; see Eq. (24) and Fig. 2 red(c).

Here, it is worth noting that, for angle-ply laminates (cases 1 and 2), since the end shortening is constant, the boundary conditions indicated in Eqs. (23) and (24) are equivalent for uniformly distributed load. For all three cases, red the side-to-thickness ratio is selected as $b/h = 50$ to represent relatively thin composite plates. redTwo aspect ratios— $a/b = 1.5$ and $a/b = 3$ are considered for angle-ply and cross-ply composite plates, respectively, unless they are specified otherwise. Although no dimensional geometric data are necessary for the present method, we chose $h = 0.02\text{m}$ for angle-ply plates and $h = 0.01\text{m}$ for cross-ply plates to facilitate the comparison with ANSYS. All composite plates are made of graphite/epoxy composites with properties: $E_1 = 137.9\text{ GPa}$, $E_2 = E_3 = 9.0\text{ GPa}$, $G_{12} = G_{13} = 7.20\text{ GPa}$, $G_{23} = 6.21\text{ GPa}$, $\nu_{12} = \nu_{13} = 0.3$, $\nu_{23} = 0.49$, and $\rho = 1450\text{kg/m}^3$ [34]. red The FEA model uses the ANSYS SHELL99 multilayered 8-noded shell element. red 60×40 elements are used for plates with aspect ratio of $a/b = 1.5$ and 60×20 elements red are used for $a/b = 3.0$.

red To verify the linear capability of the present method, we calculate the first three linear buckling loads and compare the results of the analytic solutions with those of FEA. It is verified that results calculated by the present method are identically the same as those

calculated based on the classical lamination theory in Jones [35] and Reddy [34]. As shown in Table 1, the results of the present analytic method agree with ANSYS within less than 1.82% difference. This also shows that for linear buckling analysis of thin plates, using higher-order plate theory as adopted in ANSYS SHELL99 instead of the classical plate theory will not make a significant difference.

Table 1

Linear buckling loads for antisymmetric angle-ply and cross-ply laminated plates

	Linear buckling loads, \bar{N}_{11} (N/m)	Present	ANSYS	Buckling mode ^a
Case 1	\bar{N}_{11cr1}	1.4022×10^6	1.3898×10^6	(2, 1)
	\bar{N}_{11cr2}	1.5190×10^6	1.4993×10^6	(3, 1)
	\bar{N}_{11cr3}	1.8458×10^6	1.8129×10^6	(4, 1)
Case 2	\bar{N}_{11cr1}	5.6313×10^5	5.5989×10^5	(1, 1)
	\bar{N}_{11cr2}	8.4013×10^5	8.3269×10^5	(2, 1)
	\bar{N}_{11cr3}	1.1709×10^6	1.1557×10^6	(3, 1)
Case 3	\bar{N}_{11cr1}	5.2590×10^5	5.2856×10^5	(3, 1)
	\bar{N}_{11cr2}	5.9683×10^5	5.9799×10^5	(4, 1)
	\bar{N}_{11cr3}	6.7029×10^5	6.7255×10^5	(2, 1)

^a (m, n) denotes mode shape of $A_{mn} \sin(m\pi x_1) \sin(n\pi x_2/r)$.

It is interesting to note that the critical buckling load not only depends on the out-of-plane boundary condition but also depends on the in-plane one. The plate in case 2 has the same out-of-plane boundary conditions as those of case 1 except that two of the former's longer edges are further constrained in-plane ($\Delta_{22} = 0$). Results in table 1 show that the linear buckling load of case 2 is lower than that of case 1, although the former has more edge support. The reason comes from the Poisson effect between N_{11cr} and N_{22cr} when $\Delta_{22} = 0$, see Eqs. (A-4) and (46). In fact, based upon these two equations it can be shown that for square isotropic plates ($r = 1$) with four edges simply-supported out-of-plane the critical buckling load is $N_{11cr} = 4\pi^2 D_{11}/a^2$ when the two unloaded edges are free to move in the plate plane, while it becomes $N_{11cr} = 4\pi^2 D_{11}/(a^2(1 + \nu))$ when these two edges are constrained in-plane. Clearly, the buckling load for the latter is lower than that of the former.

As a basic verification of the nonlinear capability of the present method, we apply it to analyze Stein's aluminum plate and compare with Stoll's mode jumping analysis [8]. Stein's plate consists of a uniaxially compressed four-edge simply-supported isotropic aluminum plate with dimensions of $a = 25.36$ in., $b = 4.71$ in., $h = 0.0708$ in. and material properties of $E = 10 \times 10^6$ psi., $\nu = 0.33$. Using $m \times n$ denote the mode shape of $w = W_{mn} \sin(m\pi x_1) \sin(n\pi x_2/r)$, 20 modes, $(1, 3, 5, 7, 9, 11, 13, 15, 17, 19) \times (1, 3)$, are considered in this analysis. Fig. 3 (a) shows an excellent match of the present method with Stoll's in the compressive load vs end shortening plot.

To verify the nonlinear capability of the present method for composite plates, we carry out a nonlinear analysis for the case 2 plate. The present analytic method uses 27 modes, $(1, 2, 3, 4, 5, 6, 7, 8, 9) \times (1, 2, 3)$, while the FEA uses 60×40 8-noded SHELL99 elements. To

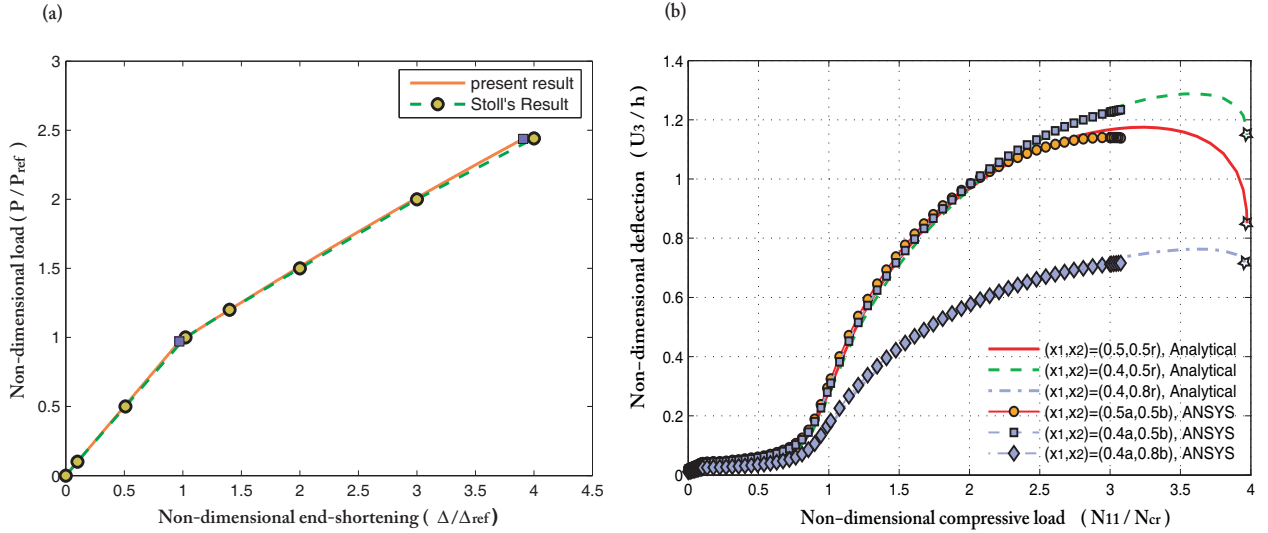


Fig. 3. Nonlinear comparison. (a) comparison with Stoll's mode jumping analysis using Stein's aluminum plate model [8], compressive load vs end shortening, $P_{ref} = 2880$ lbs., $\Delta_{ref} = 0.0219$ in.; (b) comparison with nonlinear analysis using ANSYS, compressive load vs out-of-plane deflection for case 2. Symbol star denotes the secondary bifurcation point.

facilitate the nonlinear analysis using ANSYS, we red first apply a uniformly distributed vertical pressure $f_3 = 2.3514 \times 10^3$ (N/m²) to the plate, which is equivalent to a geometry imperfection with the maximum (central) deflection of 2% of the plate thickness, i.e., $w_0(a/2, b/2) = 0.02h$; then, the coordinates is updated and pressure is removed before the start of nonlinear calculations. In analytic approach, an equivalent dimensionless pressure of red $\tilde{f}_3 = 291.0194$ is used to generate the initial deflection of the same amount. Fig. 3 (b) indicates that the present analytic results match pretty well with those of FEA until the primary postbuckling equilibrium path comes close to the secondary bifurcation point, where ANSYS fails to converge. As it will be shown latter, the analytic approach, however, can go far beyond the secondary bifurcation point and even through multiple unstable equilibrium branches and bifurcation points to capture the mode jumping phenomenon.

These several validation examples show that the present method can reliably predict the linear and nonlinear behaviors for both isotropic and composite plates. In the following, we are going to use the present method to investigate some interesting nonlinear phenomena.

4.2 Static nonlinear analysis

As it is well known that the mode jumping of compressively stressed isotropic plate is generally demonstrated by subtle mode interactions between linear buckling modes [9], [10], [11], in this work, we initiate our study of the composite plate from the linear buckling analysis.

The variations in linear buckling load with respect to various buckling modes for case 1 plate and case 2 plate are depicted in Fig. 4 over a range of plate length. Critical buckling loads for the straight-edge fixed plate are lower than those for the straight-edge free plate.

For case 1 plate shown in Fig. 4 (a), with the increasing of the aspect ratio, the lowest buckling mode will change its wave form from the (2, 1) mode to (3, 1) mode when a/b reaches 1.7 at a compound buckling point, where the lowest two buckling load curves intersect. Therefore,

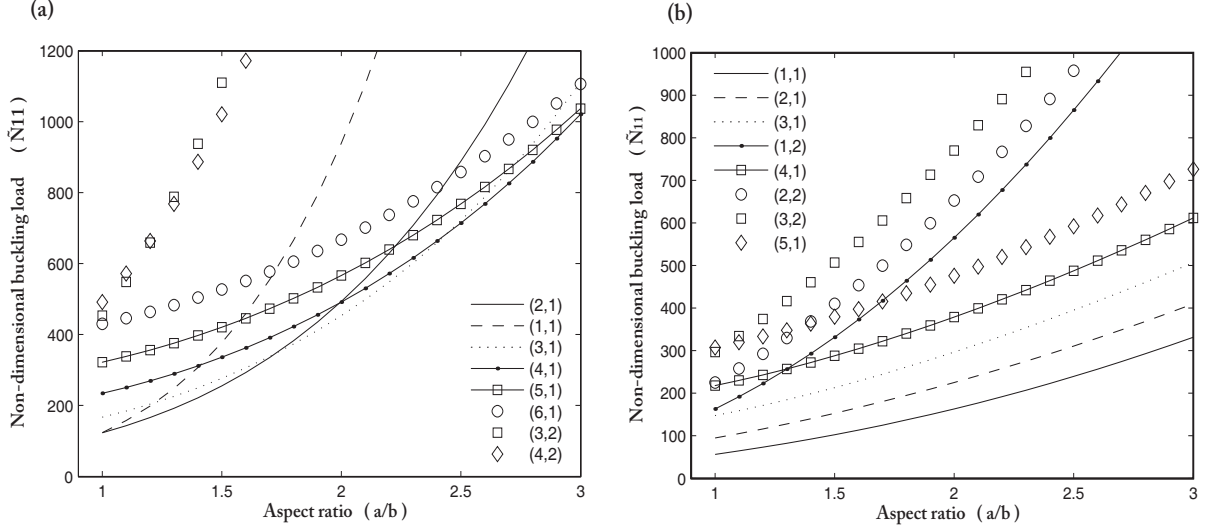


Fig. 4. Linear buckling load for simply-supported straight-edge angle-ply laminated plates. (a) case 1; (b) case 2.

it is reasonable to believe that choosing $a/b = 1.5$, an aspect ratio slightly smaller than the compound one, will encourage the occurrence of mode jumping from the (2, 1) mode to (3, 1) mode. Further investigation shows that the lowest six linear buckling modes with $a/b = 1.5$ take the form of (2, 1), (3, 1), (4, 1), (1, 1), (5, 1), and (6, 1), indicating that postbuckling behaviors of the redstraight-edge free plate may redbe dominated by the interaction of modes with several half-waves along x_1 axis and one half-wave along x_2 axis.

For case 2 plate shown in Fig. 4 (b), however, the situation is different. The lowest three load lines for this plate never intersect each other in the given range of plate length, thus no compound points exist. Such separation of linear buckling load lines implies that for a perfect redstraight-edge fixed plate the coupling effect among the lowest three primary postbuckling branches emanating from the first three linear buckling points redis not strong enough to dominate the postbuckling and the mode jumping behaviors of the plate, and more complicated mode combinations are needed to capture the snapping phenomenon.

Nonlinear quasi-static analyses are performed for case 1, case 2 and case 3 plates described in section 4.1 to investigate the postbuckling response and the secondary instability of both antisymmetric angle-ply and cross-ply plates. In all redthese cases, a complete base set consisting of 27 individual mode shapes, i.e., red(1, 2, 3, 4, 5, 6, 7, 8, 9) \times (1, 2, 3), is selected for the fully nonlinear analysis to avoid any possible misleading results caused by incorrect mode assumptions.

A nondimensional bifurcation diagram (compressive load vs out-of-plane deflection) of the stationary solution for case 1 plate is plotted in Fig. 5. Also included in this picture are typical static deformation patterns of the plate at the secondary bifurcation points (A and B) and at the corresponding point (C) on the remote stable jumped path, see Fig. 5 (b), (c) and (d). Again, a dimensionless uniformly distributed vertical pressure of $\hat{f}_3 = 291.0194$ is used to mimic the initial geometric imperfection with maximum deflection (at the center of the plate) being 2% of the thickness. The primary buckling load for the imperfect plate occurs at $N_{11b1} = 1.003N_{11cr1}$, almost the same as that of the perfect one. Two stable primary postbuckling branches emanate from this critical point and deformation patterns

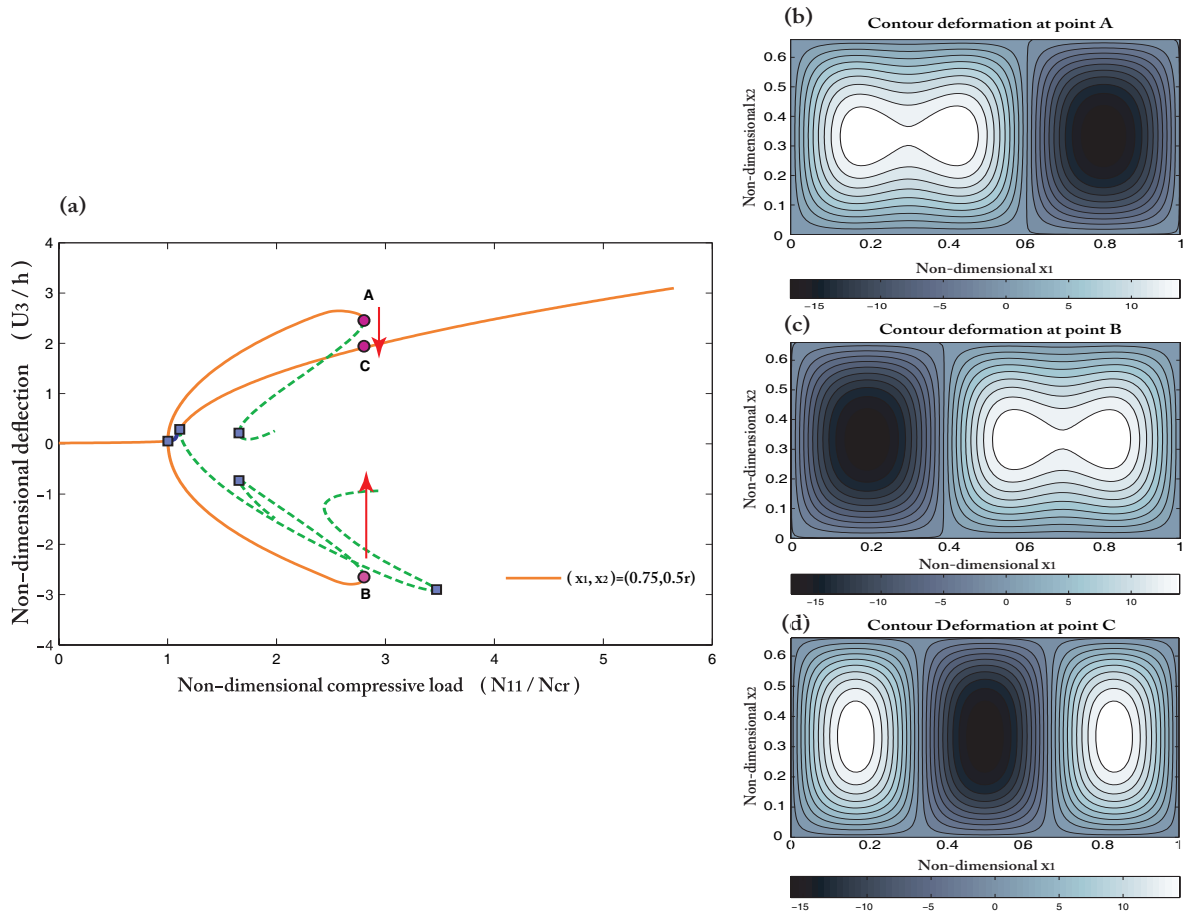


Fig. 5. Bifurcation diagram and static deformation patterns at representing points for case 1, $max(w_0) = 0.02h$. (a) bifurcation diagram; (b) and (c) deformation patterns at the secondary bifurcation points A and B, respectively; (d) deformation pattern at the corresponding point C on the remote stable jumped branch. Stable paths are shown as solid lines and unstable paths as broken lines; square symbols indicate bifurcation points.

change smoothly along these two equilibrium paths until the secondary bifurcation load is reached ($N_{11b2} = 2.795N_{11cr1}$), where two primary stable postbuckling branches lose their stabilities simultaneously and the plate experiences a dramatic change of their buckling patterns, indicating the occurrence of mode jumping.

As expected from the linear analysis, buckling patterns along the two stable primary postbuckling branches take two half wave forms along the x_1 direction and one in the x_2 . It is also interesting to note that these buckling patterns reveal some kind of symmetry – one can be obtained by flipping the other – which, as will show later, implies the existence of some intrinsic relations between stiffness matrices along these two branches. Mode jumping indicates an increase of one wave number along the x_1 direction, a phenomenon similar to Stein’s experimental observation and many numerical simulations of uniaxially compressed isotropic plates. Since both the buckling patterns before and after mode jumping are symmetric with respect to the x_1 axis, mode jumping can be qualitatively captured by using only x_1 symmetric assumed modes, such as $(1, 2, 3, 4, 5, 6, 7, 8, 9) \times (1, 3)$ or even $(1, 2, 3, 4, 5, 6) \times (1)$, notwithstanding their results not shown here.

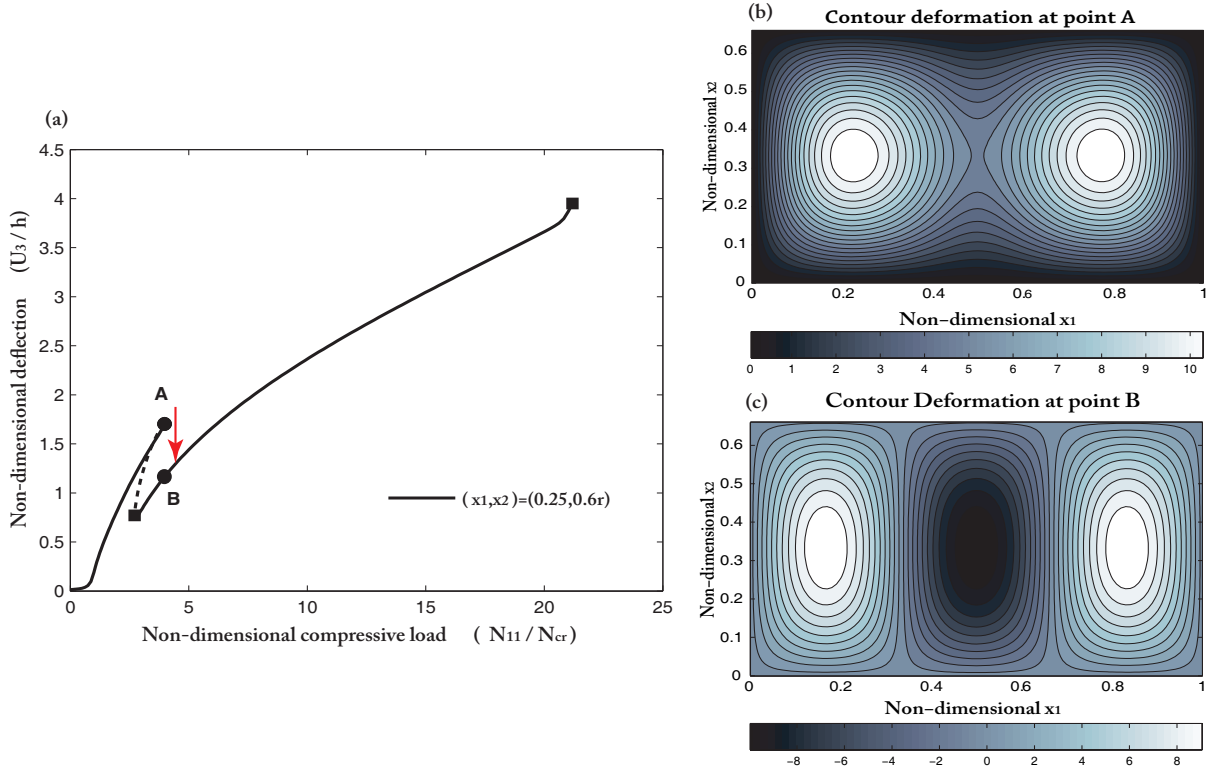


Fig. 6. Bifurcation diagram and static deformation patterns at representing points for case 2 plate, $max(w_0) = 0.02h$. (a) bifurcation diagram; (b) and (c) buckling patterns at the secondary bifurcation points A and B on stable primary postbuckling and jumped branches, respectively. Stable paths are shown as solid lines and unstable paths as broken lines; square symbols indicate bifurcation points.

Fig. 6 shows a bifurcation diagram, postbuckling patterns at the secondary buckling load on the stable primary postbuckling, and the jumped paths for case 2 plate. Again, a dimensionless uniformly distributed vertical pressure of $\tilde{f}_3 = 291.0194$ is applied to generate the maximum initial geometric imperfection of 2% of the plate thickness. Unlike case 1, this small amount of imperfection annihilates the primary bifurcation point. Mode jumping, again indicated by the increase of wave number, happens at the secondary bifurcation point when the compressive load reaches $N_{11b2} = 3.973N_{11cr1}$ where the deformation pattern of the plate encounters a significant change of wave form. Although the primary buckling mode takes (1,1) form, the buckling patterns just before the secondary bifurcation are dominated by the (2,1) shape, suggesting the subtle mode interactions. Interestingly, buckling patterns on the primary postbuckling and on the jumped branches demonstrate the symmetry with respect to both x_1 and x_2 axes, implying the possibility of using only pure symmetric modes (with respect to both x_1 and x_2 axes) to predict the qualitatively correct mode jumping response. In fact, mode base of $(1, 3, 5, 7, 9, 11) \times (1, 3)$ gives a very accurate prediction of the primary postbuckling branch, the secondary bifurcation load ($N_{11b2} = 3.974N_{11cr1}$), and the remote jumped branch. It is worth noting that caution should be paid when an incomplete set of selected mode base is used to analyze the mode jumping phenomena. Unless an a priori information of the postbuckling and jumped patterns is known, an incomplete set may lead to qualitatively incorrect results as indicated in [11] and [14].

The secondary instability or the snapping phenomenon and the corresponding alternation

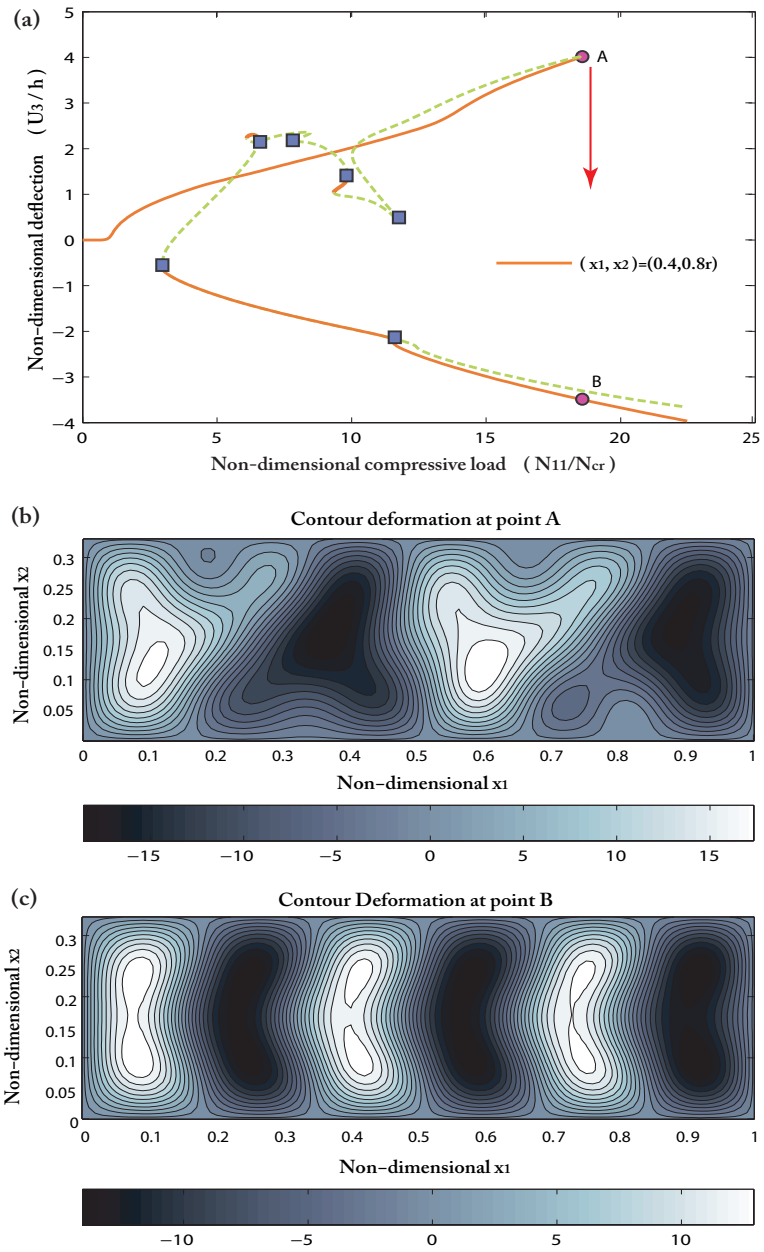


Fig. 7. Bifurcation diagram and static deformation patterns at representing points for case 3 plate. (a) bifurcation diagram; (b) and (c) buckling patterns at the secondary bifurcation points A and B on stable primary postbuckling and jumped branches, respectively. Stable paths are shown as solid lines and unstable paths as broken lines; square symbols indicate bifurcation points.

of postbuckling patterns for case 3 plate is shown in Fig. 7. As revealed in the dynamic governing equation (44), the existence of non-zero coefficients C_{B1} and C_{B2} in cross-ply laminated plate will cause pre-buckling deflections, and consequently, initial imperfection becomes unnecessary and the primary buckling point is absent even for the perfect plate. Eqs. red(44) and (B-7) also shows that antisymmetric (even) modes along x_1 is necessary to capture such pre-buckling deformation characteristic for an x_1 axially compressed cross-ply composite plate. While the nominal primary buckling load occurs at $N_{11b1} = N_{11cr1}$, the secondary instability or mode jumping takes place at $N_{11b2} = 19.476N_{11cr1}$, deeply into the postbuckling region. Much more complicated postbuckling and jumped patterns are disclosed in this picture. A scrutiny of the static deformations before and after mode jumping reveals the exhibition of pure antisymmetric (with respect to both x_1 and x_2 axes) buckling pattern on the primary postbuckling equilibrium path. In contrast, the buckling pattern on the jumped branch exhibits symmetry only with respect to the x_1 axis. Thus, a complete set of mode base (including both the odd and even modes along the x_1 and x_2 directions) is essential to accurately predict the postbuckling and mode jumping phenomenon of the cross-ply plate.

4.3 Free vibration analysis

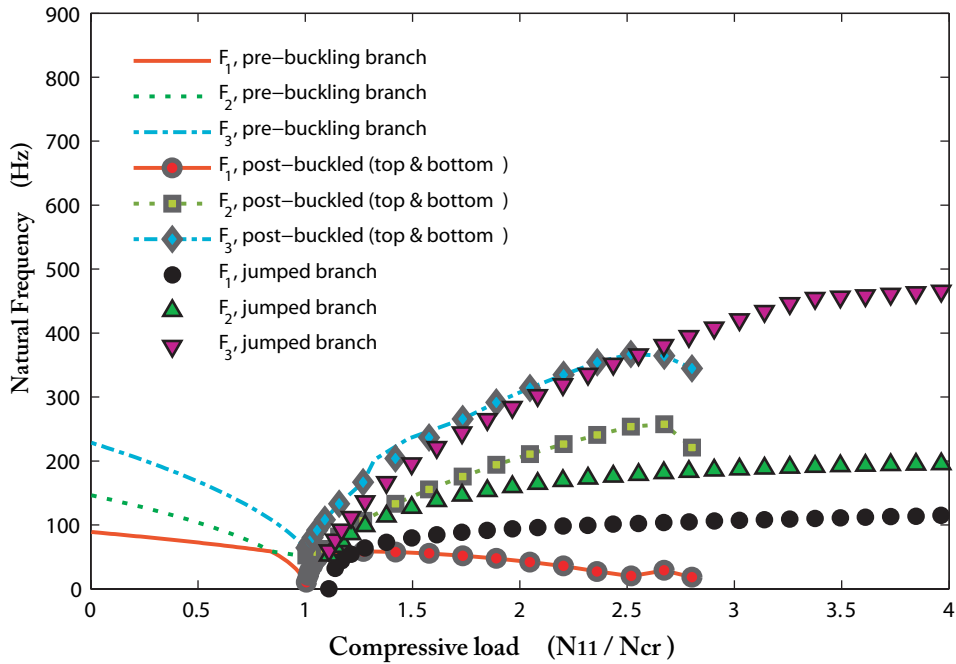


Fig. 8. Natural frequencies as a function of compressive load for case 1 plate, $max(w_0) = 0.02h$.

Fig. 8 displays the variation of the lowest three natural frequencies as a function of compressive load for the case 1 plate with maximum initial deflection as 2% of the thickness. The fundamental natural frequency drops to zero at four bifurcation points— one primary, two secondary, and the one initiating the stable jumped equilibrium path— designating the singularity of the stiffness matrix at these points. Further observation reveals the existence of a 'modal shifting' phenomenon in the pre-buckling and the primary postbuckling ranges. That is, at points when $N_{11} \approx 0.84N_{11cr1}$ and $N_{11} \approx 1.09N_{11cr1}$, the lowest two natural

frequency curves intersect and an exchange of fundamental vibration modal shape occurs. As the compressive load is increased to pass these compound frequency points, the fundamental vibration modal shape will switch to the vibration modal shape corresponding to the previously second natural frequency. However, no such 'modal shifting' scenario can be observed along the remote jumped branch. An even more interesting phenomenon can be found as we check the lowest three natural frequencies along the two stable primary post-buckling branches. These three pairs of natural frequencies along the two equilibrium paths are exactly the same, consistent with previous observations of symmetry between buckling patterns in static analysis.

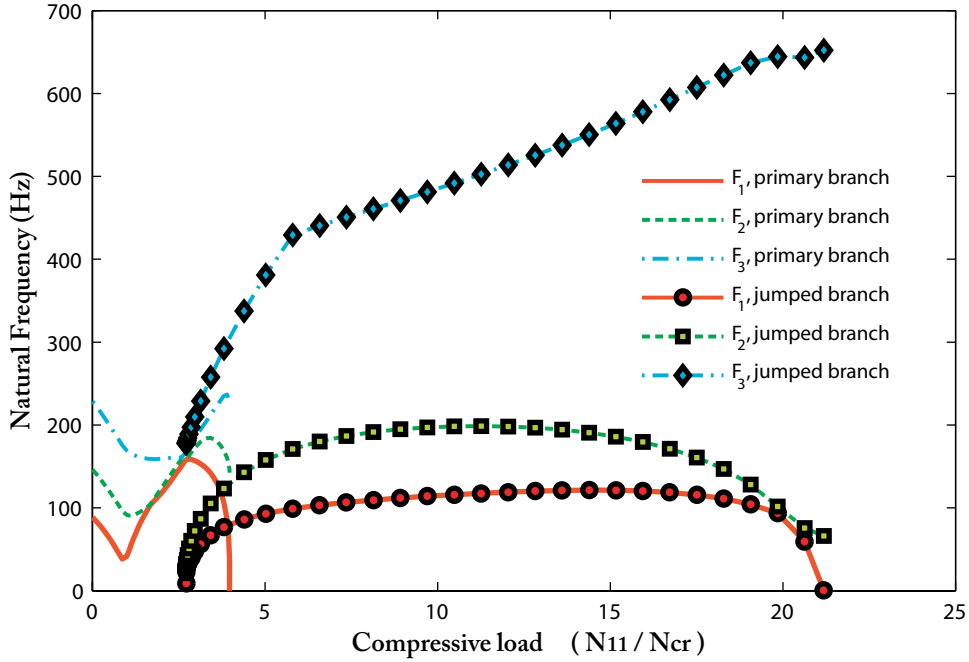


Fig. 9. Natural frequencies as a function of compressive load for case 2 plate, $\max(w_0) = 0.02h$.

The first three natural frequencies curves for case 2 plate are plotted in Fig. 9. Again, the fundamental natural frequency decreases to zero at three bifurcation points on the primary postbuckling and the jumped paths. Because of the annihilation of the primary buckling point caused by the small initial imperfection, each of the three frequency curves demonstrates a sink near $N_{11} = N_{11cr1}$ and the fundamental frequency does not drop to zero at the critical buckling load. Modal shifting phenomena are observed in both the primary postbuckling and the jumped regions (at $N_{11} \approx 1.68N_{11cr1}$, $N_{11} \approx 2.77N_{11cr1}$, and $N_{11} \approx 19.8N_{11cr1}$, respectively). When compared with the case 1 plate in the un-compressed ($N_{11} = 0$) situation, the lowest three natural frequencies for case 2 plate are the same as those of the case 1 plate. This implies that these lowest three vibration modes primarily take the form of out-of-plane bending and in-plane constraints will not affect such vibration modes when the plate is free of compression.

Finally, the lowest three natural frequencies curves for the case 3 perfect plate are plotted in Fig. 10. 'Modal shifting' is found in the pre-buckling region. Generally, the free vibration mode shape at a given equilibrium position demonstrates more morphological complexity than the static buckling deformation shape and typically more assumed modes are needed

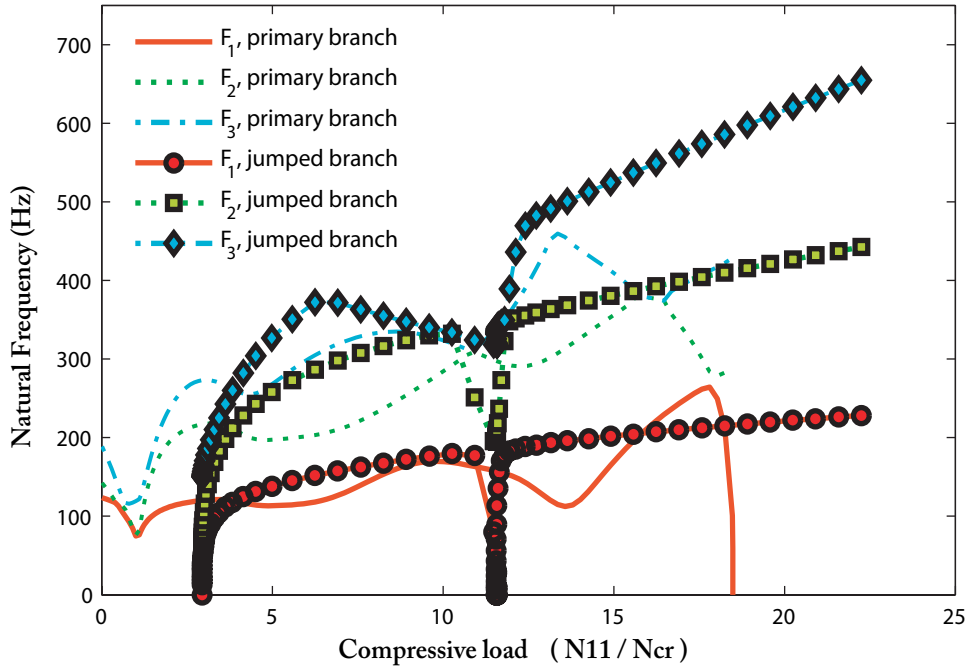


Fig. 10. Natural frequencies as a function of compressive load for case 3 plate.

to capture its geometric configuration. Interested readers may refer to [11,13,14] for detailed discussions about this topic.

5 Concluding remarks

The paper follows mathematically rigorous approaches to develop an analytic method to explore the post-buckled response including the secondary bifurcation and mode jumping of both simply-supported antisymmetric angle-ply and cross-ply laminated plates subjected to bi-axially compression. Unlike most existing approaches in the literature, kinematic relations and dynamic governing PDEs of composite plates are derived rigorously from the variational asymptotic theory, which splits the three-dimensional, anisotropic elasticity problem into a linear one-dimensional through-the-thickness analysis and a nonlinear two-dimensional “plate” analysis. The carefully selected nondimensionalization scheme generates well proposed PDEs suitable for bifurcation analysis. A novel and comparatively simpler solution procedure is developed to solve the two coupled compatibility and governing equations. The compact and explicit transformation of nonlinear PDEs to a system of nonlinear ODEs enables a systematic investigation of effects of multi-mode interactions on postbuckling response and the snapping phenomenon. Generalized Galerkin method is used to solve the boundary value problems for antisymmetric angle-ply and cross-ply laminated plates. Because the present method involves the most generalized solution procedure to handle various boundary effects, it can be readily extended to analyze simply-supported composite plates with arbitrary lamination configurations.

The comparisons between the present method and FEA demonstrate a pretty good match in their numerical results in the primary postbuckling region. While FEA loses its convergence when solution comes close the secondary bifurcation point, the present analytic approach has

the capability of exploring deeply into the post-secondary buckling realm and capture the mode jumping phenomenon for various combinations of plate configurations and boundary conditions. The critical buckling load not only depends on the out-of-plane boundary condition but also depends on the in-plane one because of the Poisson's effect when the plate has in-plane constraints. Various postbuckling patterns of different complexity are found before and after the mode jumping. Natural frequencies of composite plates are calculated along the stable primary postbuckling and the jumped equilibrium paths. The exchange of vibration modal shape or 'modal shifting' phenomenon is found for different combinations of plate configurations and boundary conditions.

Acknowledgements

This study is supported by the National Science Foundation under Grant DMI-0522908. The views and findings contained herein are those of the authors and should not be interpreted as necessarily representing the official policies or endorsement, either expressed or implied, of the National Science Foundation.

red

Appendix A. End-shortenings for angle-ply and cross-ply laminated plates

To show that the straight-edge boundary condition is satisfied for anti-symmetric angle-ply laminates, we use the following definitions for end shortenings:

$$\begin{aligned}\Delta_{11} &= \int_0^1 U_{1,1} dx_1 = \int_0^1 \left(\varepsilon_{11} - \frac{1}{2} U_{3,1}^2 \right) dx_1, & \text{end shortening along } x_1 \text{ direction,} \\ \Delta_{22} &= \int_0^r U_{2,2} dx_2 = \int_0^r \left(\varepsilon_{22} - \frac{1}{2} U_{3,2}^2 \right) dx_2, & \text{end shortening along } x_2 \text{ direction.}\end{aligned}\tag{A-1}$$

Substituting the expression of the in-plane strain in Eq.(15) and the general solution $F(x_1, x_2)$ in Eq.(28) into the first equation of Eq.(A-1), one obtains

$$\begin{aligned}\Delta_{11} &= - \left(\frac{\pi^2}{8} \right) \sum_{\substack{k,l,n \\ l \neq n}} W_{kl} W_{kn} \left[\frac{k^2(n-l)}{n+l} \cos \left(\frac{(l+n)\pi x_2}{r} \right) + \frac{k^2(n+l)}{l-n} \right. \\ &\quad \left. \cos \left(\frac{(l-n)\pi x_2}{r} \right) \right] - \left(\frac{\pi^2}{8} \right) \sum_{k,l} W_{kl}^2 k^2 - \left(\tilde{A}_{11} \bar{N}_{11} + \tilde{A}_{12} \bar{N}_{22} \right).\end{aligned}\tag{A-2}$$

It is easy to verify that $d\Delta_{11}/dx_2 = 0$, which means $\Delta_{11} = \text{constant}$. Similarly, we get $\Delta_{22} = \text{constant}$. Since the shortening along the x_1 direction is constant, its value can be easily obtained by integrating Eq.(A-2) with respect to x_2 :

$$\Delta_{11} = - \left(\frac{\pi^2}{8} \right) \sum_{k,l} W_{kl}^2 k^2 - \left(\tilde{A}_{11} \bar{N}_{11} + \tilde{A}_{12} \bar{N}_{22} \right).\tag{A-3}$$

Similarly,

$$\Delta_{22} = - \left(\frac{\pi^2}{8r} \right) \sum_{k,l} W_{kl}^2 l^2 - r \left(\tilde{A}_{12} \bar{N}_{11} + \tilde{A}_{22} \bar{N}_{22} \right). \quad (\text{A-4})$$

Similarly, for anti-symmetric cross-ply, the end shortenings along the x_1 and x_2 directions now become:

$$\begin{aligned} \Delta_{11} = & -(\bar{N}_{11} \tilde{A}_{11} + \bar{N}_{22} \tilde{A}_{12}) - \left(\frac{\pi^2}{8} \right) \sum_{k,l} W_{kl}^2 k^2 \\ & - \left(\frac{2\pi}{r^2} \right) \sum_{\substack{k,l \\ k=1,3,5,\dots}} W_{kl} \frac{(c_{6kl} \tilde{A}_{12} - \tilde{B}_{11})(kr)^2 + (c_{6kl} \tilde{A}_{11} - \tilde{B}_{12})l^2}{k} \sin \left(\frac{l\pi x_2}{r} \right), \end{aligned} \quad (\text{A-5})$$

$$\begin{aligned} \Delta_{22} = & -(\bar{N}_{11} \tilde{A}_{12} + \bar{N}_{22} \tilde{A}_{22})r - \left(\frac{\pi^2}{8r} \right) \sum_{k,l} W_{kl}^2 l^2 \\ & - \left(\frac{2\pi}{r} \right) \sum_{\substack{k,l \\ l=1,3,5,\dots}} W_{kl} \frac{(c_{6kl} \tilde{A}_{22} - \tilde{B}_{21})(kr)^2 + (c_{6kl} \tilde{A}_{12} - \tilde{B}_{22})l^2}{l} \sin(k\pi x_1). \end{aligned} \quad (\text{A-6})$$

Clearly the end shortening terms are no-longer constants.

Appendix B. red Coefficients for angle-ply and cross-ply laminated plates

red The coefficient vectors and matrices needed in dynamic equation Eq. (37) for anti-symmetric angle-ply laminates are:

$$V_{1x} = \left\{ \begin{array}{l} \frac{1}{2}, \text{ if } p = k + m; \text{ else } 0 \\ \pm \frac{1}{2}, \text{ if } p = \pm(k - m); \text{ else } 0 \end{array} \right\}, \quad V_{1y} = \left\{ \begin{array}{l} \frac{1}{2}, \text{ if } q = l + n; \text{ else } 0 \\ \pm \frac{1}{2}, \text{ if } q = \pm(l - n); \text{ else } 0 \end{array} \right\}, \quad (\text{B-1})$$

$$L_1 = (2\tilde{B}_{26} - \tilde{B}_{61})r^2 \begin{bmatrix} (k+m)^3(l+n)c_1 & (k+m)^3(l-n)c_2 \\ (k-m)^3(l+n)c_3 & (k-m)^3(l-n)c_4 \end{bmatrix} \quad (\text{B-2})$$

$$+ (2\tilde{B}_{16} - \tilde{B}_{62}) \begin{bmatrix} (k+m)(l+n)^3c_1 & (k+m)(l-n)^3c_2 \\ (k-m)(l+n)^3c_3 & (k-m)(l-n)^3c_4 \end{bmatrix},$$

$$V_{2x} = \left\{ \begin{array}{l} \frac{1}{2}, \text{ if } p = i + k + m; \text{ else } 0 \\ \pm \frac{1}{2}, \text{ if } p = \pm(i + k - m); \text{ else } 0 \\ \pm \frac{1}{2}, \text{ if } p = \pm(i - k - m); \text{ else } 0 \\ \pm \frac{1}{2}, \text{ if } p = \pm(i - k + m); \text{ else } 0 \end{array} \right\}, \quad V_{2y} = \left\{ \begin{array}{l} \frac{1}{2}, \text{ if } q = j + l + n; \text{ else } 0 \\ \pm \frac{1}{2}, \text{ if } q = \pm(j + l - n); \text{ else } 0 \\ \pm \frac{1}{2}, \text{ if } q = \pm(j - l - n); \text{ else } 0 \\ \pm \frac{1}{2}, \text{ if } q = \pm(j - l + n); \text{ else } 0 \end{array} \right\}, \quad (\text{B-3})$$

$$G_1 = \begin{bmatrix} (kn - lm)^2 & (kn + lm)^2 \\ (kn + lm)^2 & (kn - lm)^2 \end{bmatrix}, \quad E = \begin{bmatrix} E_{11} & E_{12} \\ E_{12} & E_{11} \end{bmatrix}, \quad \text{with} \quad (\text{B-4})$$

$$E_{11} = \begin{bmatrix} [(k+m)j - (l+n)i]^2 c_1 & [(k+m)j - (l-n)i]^2 c_2 \\ [(k-m)j - (l+n)i]^2 c_3 & [(k-m)j - (l-n)i]^2 c_4 \end{bmatrix}, \quad (\text{B-5})$$

$$E_{12} = \begin{bmatrix} [(k+m)j + (l+n)i]^2 c_1 & [(k+m)j + (l-n)i]^2 c_2 \\ [(k-m)j + (l+n)i]^2 c_3 & [(k-m)j + (l-n)i]^2 c_4 \end{bmatrix}. \quad (\text{B-6})$$

The coefficients, vectors, and matrices needed in dynamic equation Eq. (44) for anti-symmetric cross-ply laminates are,

$$\begin{cases} C_{B1} = \frac{4pr}{q} \tilde{B}_{11}, C_{B2} = \frac{4pr}{q} \tilde{B}_{21} & \text{if } p \text{ is even and } q \text{ is odd,} \\ C_{B1} = \frac{4q}{pr} \tilde{B}_{12}, C_{B2} = \frac{4q}{pr} \tilde{B}_{22} & \text{if } p \text{ is odd and } q \text{ is even,} \\ C_{B1} = 0, C_{B2} = 0 & \text{else,} \end{cases} \quad (\text{B-7})$$

$$\begin{cases} C_{L3} = \frac{\pi^2 pr}{8}, L_3 = \tilde{B}_{11} L_{31} + \tilde{B}_{21} r^2 L_{32} & \text{if } p+k+m \text{ is even and } q+l+n \text{ is odd,} \\ C_{L3} = \frac{\pi^2 q}{8r}, L_3 = \tilde{B}_{12} L_{31} + \tilde{B}_{22} r^2 L_{32} & \text{if } p+k+m \text{ is odd and } q+l+n \text{ is even,} \\ C_{L3} = 0, L_3 = 0 & \text{else,} \end{cases} \quad (\text{B-8})$$

$$\begin{cases} V_{3x} = V_{4x} = \left\{ \frac{4p}{p^2 - (k+m)^2}, \frac{4p}{p^2 - (k-m)^2} \right\}^T, & \text{if } p+k+m \text{ is odd} \\ V_{3x} = \{0, 0\}^T, V_{4x} = \{2, 2\}^T, & \text{if } p+k+m \text{ is even} \end{cases} \quad (\text{B-9})$$

$$\begin{cases} V_{3y} = V_{4y} = \left\{ \frac{4q}{q^2 - (l+n)^2}, \frac{4q}{q^2 - (l-n)^2} \right\}^T, & \text{if } q+l+n \text{ is odd} \\ V_{3y} = \{0, 0\}^T, V_{4y} = \{2, 2\}^T & \text{if } q+l+n \text{ is even} \end{cases} \quad (\text{B-10})$$

$$\begin{aligned} L_2 = & \tilde{B}_{21} r^4 \begin{bmatrix} (k+m)^4 c_1 & (k+m)^4 c_2 \\ (k-m)^4 c_3 & (k-m)^4 c_4 \end{bmatrix} + (\tilde{B}_{11} + \tilde{B}_{22}) r^2 \\ & \begin{bmatrix} (k+m)^2 (l+n)^2 c_1 & (k+m)^2 (l-n)^2 c_2 \\ (k-m)^2 (l+n)^2 c_3 & (k-m)^2 (l-n)^2 c_4 \end{bmatrix} + \tilde{B}_{12} \begin{bmatrix} (l+n)^4 c_1 & (l-n)^4 c_2 \\ (l+n)^4 c_3 & (l-n)^4 c_4 \end{bmatrix} \end{aligned} \quad (\text{B-11})$$

$$\begin{aligned}
G_2 &= \begin{bmatrix} (kn - lm)^2 & -(kn + lm)^2 \\ -(kn + lm)^2 & (kn - lm)^2 \end{bmatrix}, & L_{31} &= \begin{bmatrix} (l + n)^2 c_1 & (l - n)^2 c_2 \\ (l + n)^2 c_3 & (l - n)^2 c_4 \end{bmatrix} \\
L_{32} &= \begin{bmatrix} (k + m)^2 c_1 & (k + m)^2 c_2 \\ (k - m)^2 c_3 & (k - m)^2 c_4 \end{bmatrix}
\end{aligned} \tag{B-12}$$

By letting $\delta U_n = \delta U_s = \psi_{pq} = \cos(p\pi x_1) \cos((q\pi x_2)/r)$, the in-plane force boundary integration terms are

$$\begin{aligned}
&\int_{\Gamma_\sigma} \left[(N_{nn} + \bar{N}_{nn}) \delta U_n + (N_{ns} + \bar{N}_{ns}) \delta U_s \right] ds = \\
&\quad - \left(\frac{\pi^2 r}{4} \right) \sum_{k,l,m,n} W_{kl} W_{mn} \left[V_{5x}^T L_{31} V_{5y} + r V_{6x}^T L_{32} V_{6y}^T \right] \\
&\quad + \frac{\pi^2}{2} \sum_k W_{kq} c_{6kq}(kq) [1 + (-1)^{p+k}] + \frac{\pi^2}{2r} \sum_l W_{pl} c_{6pl}(pl) [1 + (-1)^{q+l}],
\end{aligned} \tag{B-13}$$

with

$$V_{5x} = \begin{Bmatrix} 1 + (-1)^{p+k+m} \\ 1 + (-1)^{p+k-m} \end{Bmatrix}, \quad V_{5y} = \begin{Bmatrix} \frac{1}{2}, & \text{if } q = l + n; & \text{else } 0 \\ \frac{1}{2}, & \text{if } q = \pm(l - n); & \text{else } 0 \end{Bmatrix}, \tag{B-14}$$

$$V_{6x} = \begin{Bmatrix} \frac{1}{2}, & \text{if } p = k + m; & \text{else } 0 \\ \frac{1}{2}, & \text{if } p = \pm(k - m); & \text{else } 0 \end{Bmatrix}, \quad V_{6y} = \begin{Bmatrix} 1 + (-1)^{q+l+n} \\ 1 + (-1)^{q+l-n} \end{Bmatrix}. \tag{B-15}$$

References

- [1] B. Audoly. Stability of traight delamination blisters. *Physical Review Letters*, 83(20):4124–4127, 1999.
- [2] M. Stein. Loads and deformation of buckled rectangular plates. NASA Technical Report R-40, National Aeronautics and Space Administration, 1959.
- [3] E. Riks, C. C. Rankin, and F. A. Brogan. On the solution of mode jumping phenomena in thin-walled shell strucures. *Computer Methods in Applied Mechanics and Engineering*, 136:59–92, 1996.
- [4] D. J. Dawe and S. Wang. Postbuckling analysis of composite laminated panels. *AIAA Journal*, 38(11):2160–2170, 2000.
- [5] B. Audoly, B. Roman, and A. Pocheau. Secondary buckling patterns of thin plate under in-plane compression. *The European Physical Journal*, 27:7–10, 2002.
- [6] N. Sridhar, D. J. Srolovitz, and B. N. Cox. Buckling and post-buckling kenetics of compressed thin films on viscous subtrates. *Acta Materialia*, 50:2547–2557, 2002.

- [7] W. J. Supple. Changes of waveform of plates in the post-buckling range. *International Journal of Solids and Structures*, 6:1244 – 1258, 1970.
- [8] F. Stoll. Analysis of the snap phenomenon in buckled plates. *International Journal of Non-linear Mechanics*, 29(2):123 – 138, 1994.
- [9] P. R. Everall and G. W. Hunt. Arnold tongue predictions of secondary buckling in thin elastic plates. *Journal of the Mechanics and Physics of Solids*, 47:2187 – 2206, 1999.
- [10] P. R. Everall and G. W. Hunt. Mode jumping in the buckling of struts and plates: a comparative study. *International Journal of Non-linear Mechanics*, 35:1067 – 1079, 2000.
- [11] H. Chen and L. N. Virgin. Dynamic analysis of modal shifting and mode jumping in thermally buckled plates. *Journal of Sound and Vibration*, 278:233 – 256, 2004.
- [12] T. Nachiketa. Secondary buckling of compression-loaded composite plates. *AIAA Journal*, 40(10):2120–2126, 2002.
- [13] H. Chen and L. N. Virgin. Finite element analysis of post-buckling dynamics in plates. part ii: A non-stationary analysis. *International Journal of Solids and Structures*, 43(13):4008–4027, 2006.
- [14] H. Chen and L. N. Virgin. Finite element analysis of post-buckling dynamics in plates. part i: An asymptotic approach. *International Journal of Solids and Structures*, 43(13):3983–4007, 2006.
- [15] G. B. Chia. Large deflection of laminated composite plates. *Composite Science and Technology*, 42:349–360, 1991.
- [16] K. K. Shukla and Y. Nath. Analytical solution for buckling and post-buckling of angle-ply laminated plates under thermomechanical loading. *International Journal of Non-linear Mechanics*, 36:1097–1108, 2001.
- [17] G. P. Zou and S. S. E. Lam. Post-buckling analysis of imperfect laminates using finite strips based on higher-order plate theory. *International Journal for Numerical Methods in Engineering*, 56:2265–2278, 2003.
- [18] D. W. Jensen and P. A. Lagace. Influence of mechanical couplings on the buckling and post-buckling of anisotropic plates. *AIAA Journal*, 26(10):1269–1277, 1998.
- [19] A. C. Orifici, R. S. Thomson, A. J. Gunnion, R. Degenhardt, H. Abramovich, and J. Bayandor. Benchmark finite element simulations of postbuckling composite stiffened panels. In *Proceedings of the 11th Australian International Aerospace Congress*, Melbourne, Australia, March 2005.
- [20] A. K. Noor and S. W. Burton. Assessment of shear deformation theories for multilayered composite plates. *Applied Mechanics Review*, 41(1):1 – 13, 1989.
- [21] A. K. Noor and S. W. Burton. Assessment of computational models for multilayered composite shells. *Applied Mechanics Review*, 43(4), April 1990.
- [22] A. K. Noor and M. Malik. An assessment of five modeling approaches for thermo-mechanical stress analysis of laminated composite panels. *Computational Mechanics*, 25:43–58, 2000.
- [23] J. N. Reddy. A simple higher-order theory for laminated composite plates. *Journal of Applied Mechanics*, 51:745 – 752, 1984.

- [24] M. Touratier. An efficient standard plate theory. *International Journal of Engineering Science*, 29:901 – 916, 1991.
- [25] M. DiSciua. Development of anisotropic multilayered shear deformable rectangular plate element. *Computers and Structures*, 21:789 – 796, 1985.
- [26] Y. B. Cho and R. C. Averill. First-order zig-zag sublaminated plate theory and finite element model for laminated composite and sandwich panels. *Composite Structures*, 50:1 – 15, 2000.
- [27] V. L. Berdichevsky. Variational-asymptotic method of constructing a theory of shells. *PMM*, 43(4):664 – 687, 1979.
- [28] W. Yu, D. H. Hodges, and V. V. Volovoi. Asymptotic construction of Reissner–like composite plate theory with accurate strain recovery. *International Journal of Solids and Structures*, 39:5185 – 5203, 2002.
- [29] D. H. Hodges, A. R. Atilgan, and D. A. Danielson. A geometrically nonlinear theory of elastic plates. *Journal of Applied Mechanics*, 60(1):109 – 116, March 1993.
- [30] D. H. Hodges, W. Yu, and M. Patil. Geometrically-exact, intrinsic theory for dynamics of moving composite plates. In *Proceedings of the 47th Structures, Structural Dynamics and Materials Conference*, Newport, Rhode Island, May 1 – 4 2006. AIAA.
- [31] D. G. Shaeffer and M. Golubttsky. Boundary conditions and mode jumping in the buckling of rectangular plates. *Communications in Mathematical Physics*, 69:59 – 92, 1979.
- [32] S. Ilanko. Vibration and post-buckling of in-plane loaded rectangular plates using a multiterm galerkin’s method. *ASME Journal of Applied Mechanics*, 69(589 – 592), 2002.
- [33] E. H. Doedel, A. R. Champneys, T. F. Fairgrieve, Y. A. Kuznetsov, B. Sandstede, and X.-J. Wang. Auto 97: Continuation and bifurcation software for ordinary differential equations. Technical Report, Department of Computer Science, Concordia University, Montreal, Canada, 1997.
- [34] J. N. Reddy. *Mechanics of Laminated Composite Plates and Shells, Theory and Analysis*. CRC Press, second edition, 2004.
- [35] R. M. Jones. *Mechanics of Composite Materials*. Taylor & Francis, second edition, 1999.